Double layer metal-based metasurface stack for light beam steering

Robin Kaißner
Kirchhoff-Institute for Physics,
University of Heidelberg

June 6, 2018

Abstract

In this work a double layer metasurface stack is reported, wherein one metasurface layer shows fully functional behaviour while the other metasurface layer is electromagnetically cloaked at the same time for near-infrared wavelengths. The metasurface stack consists of two gold nanorod based metasurfaces of different polar angle distributions on top of a glass substrate, separated by a few nanometer thick spacer polymer layer. It is shown that the coupling between the two metasurfaces leads to effects, which cannot simply be attributed to the sum of the individual single metasurfaces. This observation is used to develop and introduce a post-fabrication dynamical magnesium/gold double layer metasurface stack, capable of steering a light beam into two arbitrary, independent and switchable directions.

Contents

1 Introduction **3**

2 Theoretical Background **5**
- 2.1 Localized surface plasmon-polariton excitations in metal nanostructures . . . 5
- 2.2 The generalized law of refraction and reflection . . . 11
- 2.3 Pancharatnam-Berry metasurface for anomalous refraction . . . 16

3 Methods **21**
- 3.1 Nanofabrication . . . 21
  - 3.1.1 Spin coating process . . . 21
  - 3.1.2 Electron-beam lithography . . . 22
- 3.2 Scanning electron microscopy . . . 29
- 3.3 Optical measurements . . . 29
  - 3.3.1 Experimental setup . . . 29
  - 3.3.2 Single wavelength measurements . . . 30
- 3.4 Simulations . . . 32

4 Results and Discussion **36**
- 4.1 Single layer metasurface . . . 37
  - 4.1.1 Pancharatnam-Berry phase shift and conversion efficiency of gold nanorod array . . . 37
  - 4.1.2 Metasurface for anomalous refraction . . . 43
- 4.2 Double layer metasurface stack . . . 49
  - 4.2.1 Conversion efficiency of two stacked gold nanorod arrays 49
  - 4.2.2 Phase shift dependence on Φ_{rel} . . . 56
  - 4.2.3 Double layer metasurface stack for anomalous refraction 61
- 4.3 Switchable metasurface stack for light beam steering . . . 74
  - 4.3.1 Conversion efficiency and phase shift of Mg/Au metal-hybrid array stack . . . 75
  - 4.3.2 Simulations of Mg/Au metal-hybrid metasurface stack 82

5 Summary, Conclusions and Outlook **84**

Supplement **87**

Acknowledgement **88**

1 Introduction

The physical concept of metasurfaces gained a lot of attention recently for their various applications in the field of ultra-thin optics. Conventional optical components rely on the propagation of light through a bulky material of thickness larger than the wavelength of the light, to be able to engineer its phase, polarization or amplitude. Metasurfaces provide the opportunity to shape the phase, polarization and amplitude of light with subwavelength resolution and also within subwavelength propagation distance [5][17][2], making them, along with their relatively easy fabrication process, a promising solution for ultra-thin planar optical devices.

Basically a metasurface is a tailored 2D array of nanoscatterers, interacting and shaping the incident electromagnetic fields at the interface with subwavelength spatial resolution. Plasmonic metasurfaces have been reported, where the nanoscatterers are metallic structures such as gold nanorods, V-shaped antennas, split-ring resonators and many more [12][17][11][16]. In addition, dielectric metasurfaces, which are using dielectric scatterers such as TiO_2 or silicon have been demonstrated with the advantage of low ohmic losses [2][10]. Reported functionalities are flat meta lenses [10], meta holograms [12], polarization splitters [16] and many more. The named applications are realized by individual single layer metasurfaces of different fabrication details.

In this work a double layer metasurface stack is investigated, consisting of two individual metasurfaces on top of each other, at nanometer distance. The study and understanding of stacked metasurfaces on nanometer scale under illumination of circularly polarized light is important to built flat optic devices, which are able to combine several optical functionalities of individual metasurfaces within a single device. The stacked configuration offers new effects, which cannot be realized by a combination of two metasurfaces in one layer, which has been demonstrated already with the help of shifted unit cells [16].

At the beginning, individual single layer gold metasurfaces, fabricated by electron-beam lithography, are investigated, subsequently a double layer metasurface stack containing the investigated single layer metasurfaces is discussed. At the end a concept is presented, to achieve post-fabrication dynamical light beam steering with the help of the reported double layer metasurface stack. Therefore, each individual metasurface contained in the stacked configuration is tailored in order to refract incident circularly polarized light in

individual directions. By the use of magnesium nanorods within the upper metasurface and gold nanorods within the lower metasurface, a switching between the two refraction direction is possible upon hydrogen exposure, which induces a reversible phase transition of magnesium to the dielectric material magnesium hydrid [15][3][8][7], while the gold keeps its metallic state.

2 Theoretical Background

In this chapter the related theoretical physics will be presented. First the particle plasmons are introduced, which are the key elements of the light-matter interaction within a plasmonic metasurface. Thereafter a deduction of the generalized law of refraction is presented, forming the basic theory of light beam deflection with the help of metasurfaces, using the anomalous refraction. At the end of the chapter the context of metasurfaces designed to realize the anomalous refraction is given.

2.1 Localized surface plasmon-polariton excitations in metal nanostructures

Bulk metals, metal-dielectric interfaces and metal particles show interesting optical properties mainly due to the presence of electromagnetic resonances, which are related to collective quasi-free conduction-band electron oscillations named 'plasmons'. The different boundary conditions for the electrical fields associated with plasmons in bulk metals, metal-dielectric interfaces or metal particles lead to different conditions for their occurrence for these three cases [14].
In bulk metals, collective density oscillations of quasi-free conduction band electrons are called volume plasmons. At a metal-dielectric interface the excitation of surface plasmons is possible, which are non-propagating collective electron density oscillations at the surface of the metal. This charge motion always creates electromagnetic fields outside of the metal as well as (decaying fields) inside. The excitation of a surface plasmon at a metal-dielectric interface, together with the associated electromagnetic fields is called a surface plasmon-polariton. It is a non-radiative, propagating wave along the interface, which is characterized by a electronic charge motion at the surface of the metal structure (surface plasmon) as well as a guided electromagnetic wave in the dielectric medium (polariton). For metal particles of subwavelength dimension the excitation is confined to the particle's surface dimensions, called then a localized surface plasmon-polarition (LSPP).
The LSPP excitations in subwavelength sized metal particles and their coupling to neighboring particles' excitations is important for the understanding of optical responses of surfaces, which are structured with such subwavelength sized metal resonators. This is due to the fact that the LSPP can be excited by light, while the bulk plasmons can not, neither can the surface

plasmon-polaritons without applying special experimental setups.
The energy of possible localized surface plasmon resonances (LSPR) in nanostuctures is highly dependent on the dimensions of the structure, and therefore adjustable by fabricating appropriate structure dimensions [4][9]. For isotropic nanoparticles like spheres, a single resonance is observed, which spectral position mainly depends on the radius, the material of the sphere and the surrounding medium [13]. The resonance is observed as a peak in the light absorption and scattering spectrum. The spectrum of anisotropic structures can show a couple of distinct plasmonic resonances, corresponding to the different resonance conditions for each direction. A nanorod, for example, shows a longitudinal and transversal plasmonic resonance, which spectral positions ω_l and ω_t depend on the rod length and the rod width, respectively. They are excited by appropriately polarized light, meaning the electric field vector has to have non-vanishing components along the electron oscillation directions.
Figure (1) shows a schematic of a localized particle plasmon excitation within a metal nanorod, as well as a corresponding light scattering cross-section. The peak extinction as well as the width of the resonance peak is dependent on the degree of damping of the particle plasmon excitation and the volume of the particle. Localized particle plasmons decay via two channels, either radiatively or by creating an electron-hole pair, so called intra- and interband transitions of the metal electrons [14].

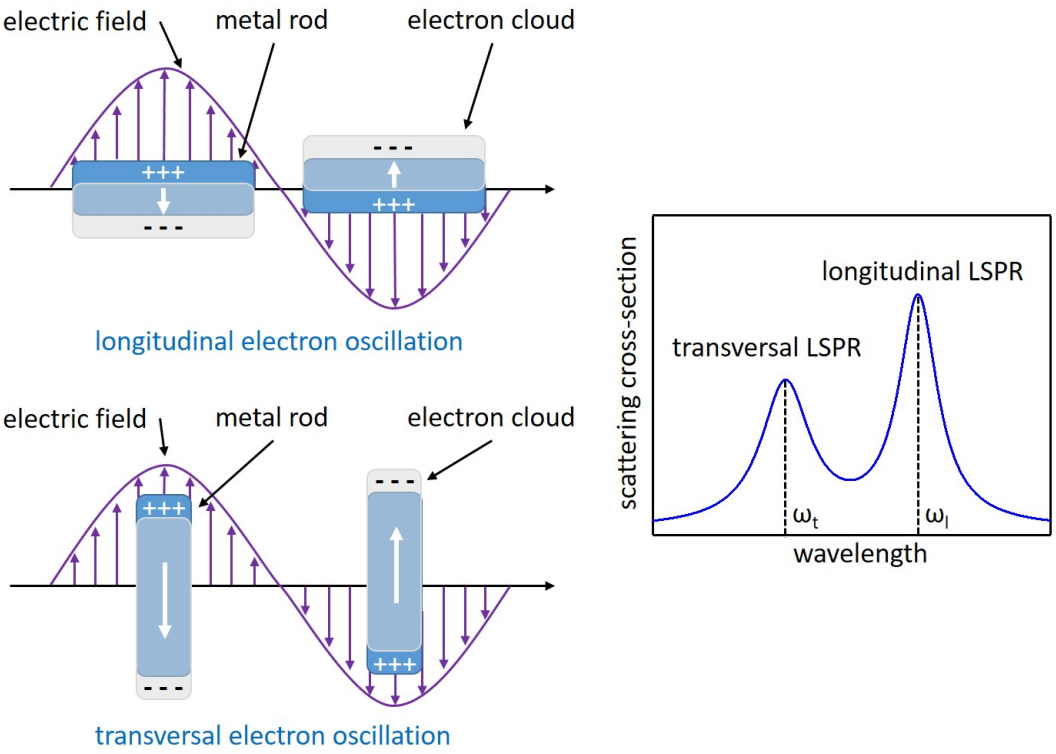

Figure 1: Schematic illustration of a localized particle plasmon resonance in gold nanorods (left) and the corresponding light scattering cross-section (right). The electric field (purple) of an incident light wave induces a collective charge motion within the nanorods (blue). Depending on the orientation of the rod, the electron cloud (white) oscillates along the longitudinal or transverse axis of the rods, which may lead to two distinct resonance peaks.

Quasistatic approximation The theoretical description of the light absorption, scattering and extinction of metallic nanorods of subwavelength dimensions can be approximated by a quasi-static electrodynamic approach, in which the dimensions of the particle are sufficiently small, so that the phase of the incident light wave is assumed to be constant throughout the domains of interest. A further approximation describes the nanorod as an ellipsoidal particle, a prolate spheroid with axis $a>b=c$. The following mathematical description is related to the work about light scattering by small particles from Bohren and Huffman in 1982 and reference [14]. A schematic illustration of a metallic spheroid in an external electric field is shown in figure (2). The polarization of the particle and its resulting internal electric field is presented.

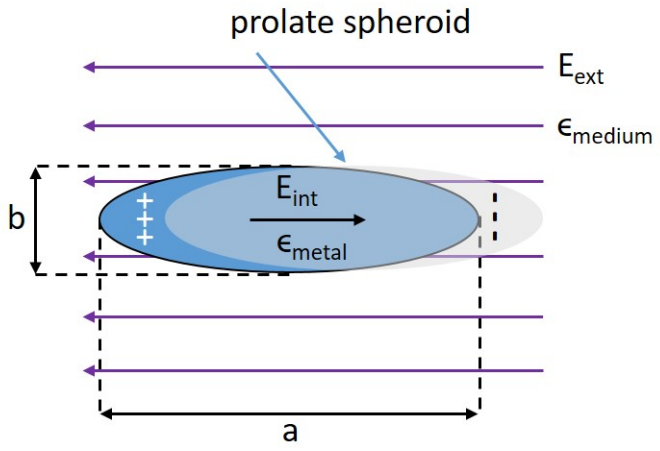

Figure 2: Schematic drawing of a prolate spheroid (blue) in a constant external electric field (purple), which induces a polarization by displacing the electron cloud (white), resulting in an internal electric field within the metal spheroid. The long axis is named a and the short axis b. The dielectric constants ϵ of the medium as wall as the metals are depicted as well.

For a spheroidal particle, the polarizability α along the axis i is given by

$$\alpha_i(\omega) = \frac{V\epsilon_0}{L_i}\frac{1-\epsilon_r(\omega)}{(1/L_i-1)+\epsilon_r(\omega)}, \tag{1}$$

wherein $\epsilon_r = \epsilon_{\text{metal}}(\omega)/\epsilon_{\text{medium}}$ is the relative dielectric function, V is the vol-

ume of the particle and L is a geometrical factor. The geometrical factor of a prolate spheroid along its long axis a is given by

$$L_a = \frac{1-e^2}{e^2}\left(-1 + \frac{1}{2e}\ln\frac{1+e}{1-e}\right) \tag{2}$$

with the eccentricity

$$e^2 = 1 - \frac{b^2}{a^2}, \tag{3}$$

including the aspect ratio a/b of the spheroid. It holds that $L_a + L_b + L_c = 1$ and with $L_b = L_c$ the relation

$$L_b = L_c = \frac{1-L_a}{2} \tag{4}$$

follows. For a nanosphere L_i is the same for every axis and takes the value of 1/3. The scattering and absorption cross-section can be calculated with the help of the polarizability α to

$$C_{\text{sca}} = \frac{8\pi^3}{3\lambda^4}|\alpha/\epsilon_0|^2 \tag{5}$$

$$C_{\text{abs}} = \frac{2\pi}{\lambda}\text{Im}(\alpha/\epsilon_0). \tag{6}$$

The extinction cross-section is defined as

$$C_{\text{ext}} = C_{\text{sca}} + C_{\text{abs}}. \tag{7}$$

Coupling A coupling between two longitudinal LSPR-excitations is possible for sufficiently small distance of two nanorods. A coupling scheme for LSPRs within two vertically stacked parallel nanorods at nm distance d is presented in figure (3a) . A possible scattering cross-section is depicted below (b). The single LSPRs couple to new modes, both shifted in energy in respect

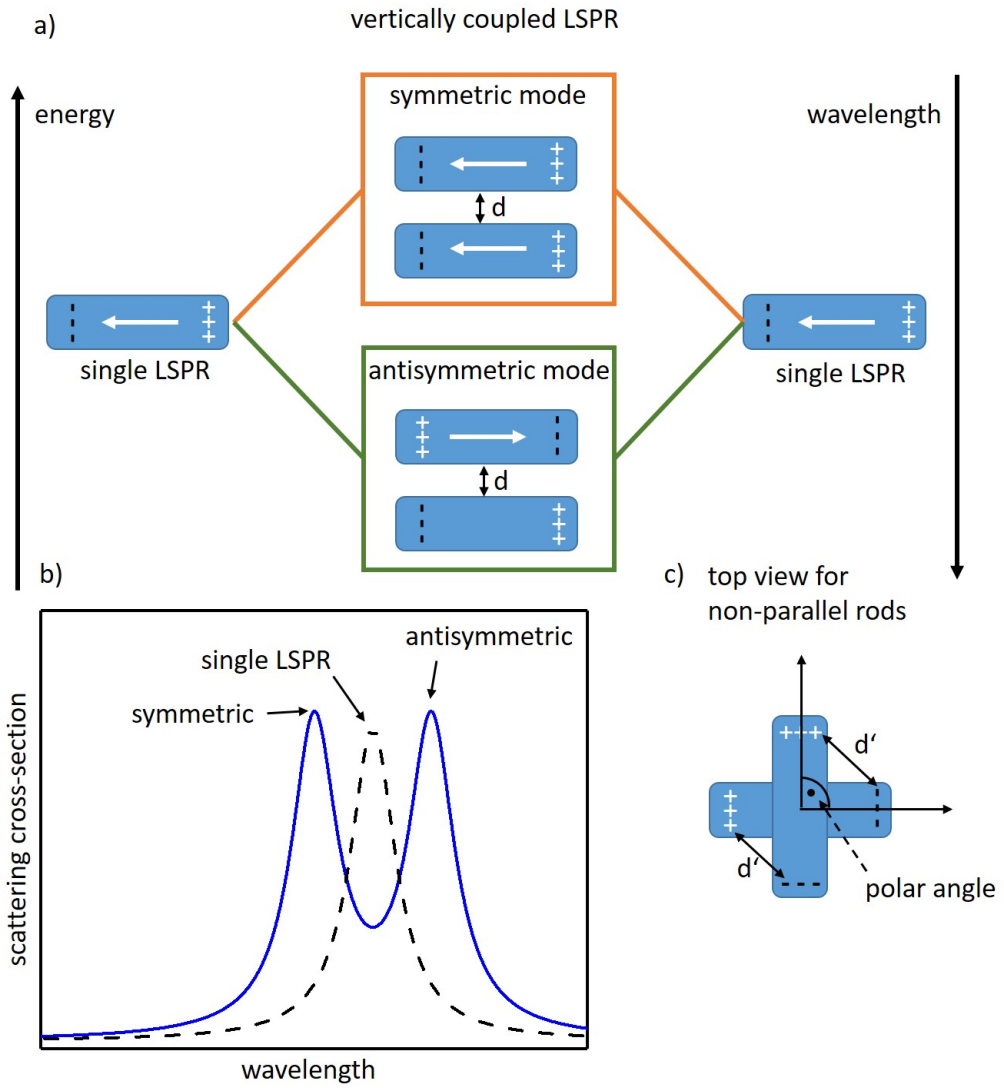

Figure 3: Illustration of the energy splitting of the coupling modes of two individual single localized surface plasmon resonances (LSPR) in metal nanorods, which are located above each other at a nm distance (top). The corresponding scattering cross-section is shown below, showing the cross-section for the coupled case (blue) as well as the cross-section for the single LSPR mode of the individual nanorod without coupling to a neighboring rod (dashed).

to the single LSPR-mode. For the symmetric mode the electron oscillation in both nanorods is in phase, while for the antisymmetric case the phase is shifted by π (antiphase). The symmetric mode has a larger energy, since the coulomb-repulsion between the electrons within the two rods is larger on average compared to the antisymmetric mode, which can be understood with the help of the illustrated charge locations. For the symmetric mode, charges of same sign are neighboring, increasing the potential energy, while for the antisymmetric mode, charges of opposite sign are neighboring, decreasing the energy.
The energy shift of the coupled modes as well as their extinction depends also on the polar angle between the two rods. To understand this, a top view is given for an example of perpendicular rods (polar angle 90°) (c). For the parallel case the coupling is most efficient, since the both rod ends are very close to each other at distance d. The mode splitting is large due to the high energy gain of the antisymmetric mode and the high energy loss of the symmetric mode. The splitting decreases as the polar angle is increased, since the distance between the rod ends increases, leading to a loss of influence of the attraction and repulsion effects of the electrons. The mode splitting is minimal for perpendicular rods, since the ends of the two rods are at a maximum distance d' for this case. A longitudinally coupled LSPR excitation in two non-parallel rods is possible for circularly polarized incident light with an appropriate wavelength.
At the end of this section it should be mentioned, that two coupled nanorods located next to each other instead of above each other show opposite behaviour, the antisymmetric mode is the high energy mode here. Since this work deals with vertically stacked metasurfaces, which show the vertical coupling between the nanorods, this case is neglected at this point and simply mentioned.

2.2 The generalized law of refraction and reflection

To use a metasurface for light beam deflection into an arbitrary direction, independently from the incident angle, the generalized law of refraction plays an important role. It is capable of expressing the relation between light deflection angle and actual fabrication design of the metasurface.
The generalized law of refraction can be deduced by using Fermat's principle of stationary phase and including an additional term for an abrupt phase discontinuity at the interface of two isotropic media with refractive index n_i

and n_r. The deduction presented in the following is related to the work of Nanfang Yu et al. in 2011 [17]. The actual path that light takes, is the one of minimal gathered phase, therefore the derivative of the phase $\int_A^B d\varphi(\vec{r})$ accumulated between two points A and B should be zero with respect to infinitesimal variation of the light path. Allowing for an abrupt phase discontinuity $\phi(x)$ at the interface the total phase can be written as

$$\phi(x) + \int_A^B d\varphi(\vec{r}) = \phi(x) + \int_A^B \vec{k} \cdot d\vec{r} \tag{8}$$

where $\vec{k}$ is the wave vector of the light.
Figure (4) shows a scheme of the two light paths between A and B. The phase difference between two infinitesimal close paths to the actual light path has to be zero, which leads to the equation

$$\phi(x) + \int_A^B \vec{k} \cdot d\vec{r} - \left[\phi(x + \Delta x) + \int_A^B \vec{k} \cdot d\vec{r}\right] = 0. \tag{9}$$

The integrals can be split respectively,

$$\int_A^B \vec{k} \cdot d\vec{r} = \int_A^C \vec{k} \cdot d\vec{r} + \int_C^D \vec{k} \cdot d\vec{r} + \int_D^B \vec{k} \cdot d\vec{r} \tag{10}$$

and

$$\int_A^B \vec{k} \cdot d\vec{r} = \int_A^{C'} \vec{k} \cdot d\vec{r} + \int_{C'}^{D'} \vec{k} \cdot d\vec{r} + \int_{D'}^B \vec{k} \cdot d\vec{r}, \tag{11}$$

wherein the integration borders are named according to the schematic drawing in figure (4). Assuming the points A and B to be in the xz-plane and far away from the interface and the distance Δx between C and D' to be infinitesimal small, the approximations

$$\int_A^C \vec{k} \cdot d\vec{r} \approx \int_A^{C'} \vec{k} \cdot d\vec{r} \tag{12}$$

and

$$\int_D^B \vec{k} \cdot d\vec{r} \approx \int_{D'}^B \vec{k} \cdot d\vec{r} \tag{13}$$

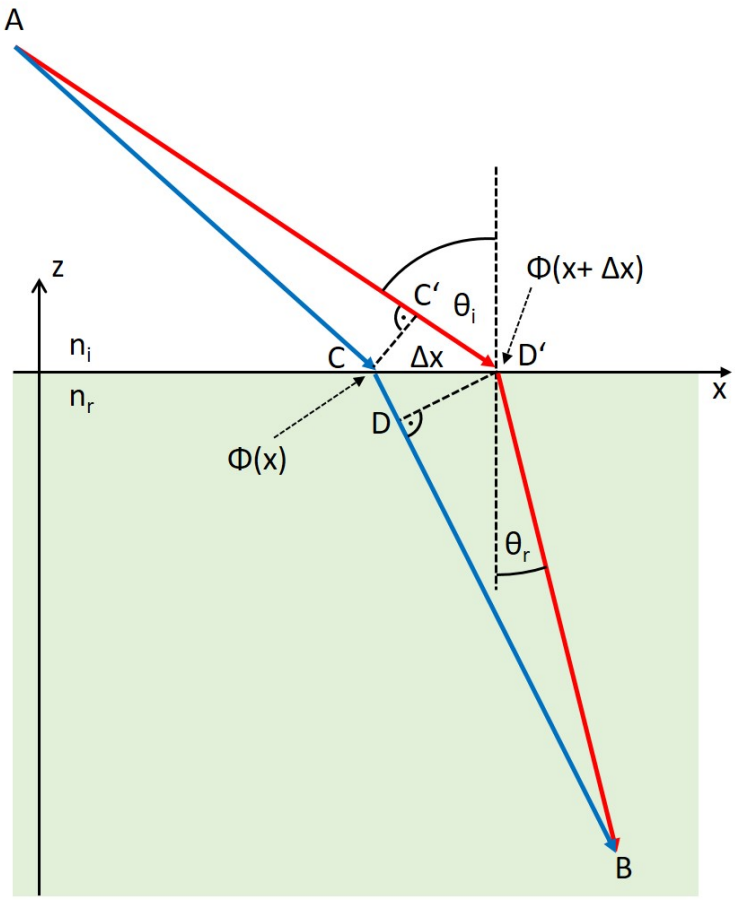

Figure 4: Schematic presentation of light refraction at a interface of two media with refractive index n_i and n_r. Two light paths (red and blue) are shown, which are infinitesimal close to the actual light path between points A and B. A position dependent phase shift $\Phi(x)$ is added to the light at the interface. The incident and refraction angles are Θ_i and Θ_r, respectively.

hold. Inserting them into (9) leads to

$$\phi(x) + \int_C^D \vec{k} \cdot d\vec{r} - \phi(x + \Delta x) - \int_{C'}^{D'} \vec{k} \cdot d\vec{r} = 0. \tag{14}$$

Assuming a plane wave of vacuum wavelength λ_0 at incident angle θ_i and refraction angle θ_r, with the vacuum wave vector $\vec{k}_0 = \frac{2\pi}{\lambda_0} \cdot \vec{e}_k$ lying in the xz-plane as well, (14) can be expressed as

$$\phi(x) + \frac{2\pi}{\lambda_0} n_r \cdot \sin(\theta_r)\Delta x - \phi(x + \Delta x) - \frac{2\pi}{\lambda_0} n_i \cdot \sin(\theta_i)\Delta x = 0. \tag{15}$$

Taylor-expanding

$$\phi(x + \Delta x) = \phi(x) + \frac{d\phi(x)}{dx}\Delta x \tag{16}$$

up to first order, and dividing the whole equation by Δx, results in the generalized Snell's law of refraction

$$n_r \sin(\theta_r) - n_i \sin(\theta_i) = \frac{\lambda_0}{2\pi} \frac{d\phi(x)}{dx}. \tag{17}$$

For $\phi(x) =$ constant, we end up with the conventional Snell's law, where the refraction angle is related to the incident angle. For $\phi(x)$ linear in x the refraction angle can have arbitrary values, not only depending on the incident angle, but on the value of the constant phase gradient $\frac{d\phi(x)}{dx}$ along the interface as well. For fixed incident angle it is possible to achieve arbitrary refraction angles by designing a suitable constant phase gradient along the interface of the two media. This can be achieved by a appropriate design of a metasurface.
In addition to the generalized equation of refraction, there can be derived a generalized equation of reflection as well, by applying a similar concept [17]:

$$\sin(\theta_{\text{refl}}) - \sin(\theta_i) = \frac{\lambda_0}{2\pi n_i} \frac{d\phi(x)}{dx}. \tag{18}$$

Refraction at second interface In the following, some further assumptions will be made to simplify the generalized refraction equation for this work. First we will treat the case of normal incidence $\theta_i = 0$ and furthermore the total refraction angle is calculated after the light is conventionally refracted a second time at the lower interface, leaving the medium n_r and entering again into the medium n_i, which we assume to be air. A schematic illustration is depicted in figure (5). The anomalous refraction angle for normal incidence is given by

$$\theta_r = \arcsin\left(\frac{\lambda_0}{2\pi n_r}\frac{d\phi(x)}{dx}\right). \tag{19}$$

For the second interface, which is assumed to be parallel to the first, θ_r is the new incident angle. The conventional refraction can be calculated by inserting (19) into Snell's law,

$$n_r \cdot \sin(\theta_r) = n_i \cdot \sin(\theta_{\text{tot}}) \tag{20}$$

leading to the total refraction angle

$$\theta_{\text{tot}} = \arcsin\left(\frac{\lambda_0}{2\pi}\frac{d\phi(x)}{dx}\right). \tag{21}$$

In this work, refraction angle measurements of monochromatic light will be performed on metasurfaces on top of a glass substrate under ambient conditions and normal incidence. This setup fulfills all of the above discussed assumptions and finally leads to θ_{tot} as the quantity of observation.

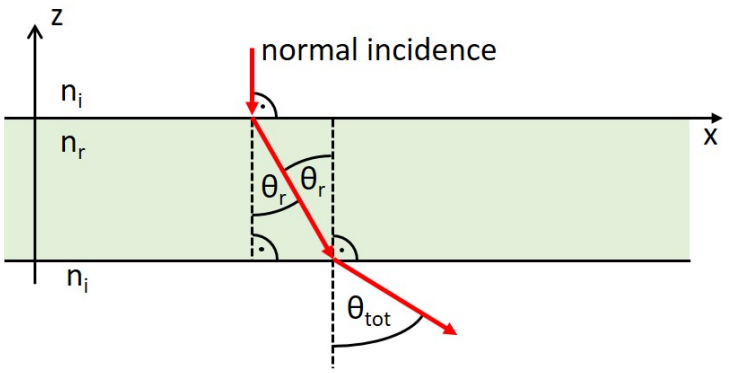

Figure 5: Schematic presentation of light refraction at an interface of two media with refractive index n_i and n_r for the case of normal incident light. The upper interface is refracting the light anomalously, while at the lower interface the light is conventionally refracted, leading to a total deflection angle Θ_{tot}.

2.3 Pancharatnam-Berry metasurface for anomalous refraction

A plasmonic metasurfaces is basically a flat substrate surfaces, which is structured with a 2D array of metallic scatterers of subwavelength dimensions and separation, allowing the control of polarization, phase and amplitude of incident electromagnetic waves locally and therefore with subwavelength resolution. There are several possibilities of controlling the phase of the incident light locally with the help of the nanoscatterers.
One is to use a fixed incident wavelength and adjust the length of the scatterers locally. The incident light couples to the metallic statterers, inducing surface plasmons together with their associated surface currents. These oscillating currents lead to electromagnetic waves themselves, since accelerated charges radiate (scattered light), which has a certain phase shift in respect to the incident driving electromagnetic light wave. The phase shift is dependent on the degree of matching of the incident light wavelength and the plasmon resonance wavelength, which is dependent on the geometry of the scatterer [17]. Therefore, the scattered light's phase can be designed with the help of the metallic scatterers' length. Another possibility to use this so called 'optical phase' is the local variation of incident wavelengths for fixed scatterer

lengths, which utilizes the degree of matching of the plasmon resonance and incident wavelength as well. Nevertheless, there must be utilized additional effects like coupling of scatterers and geometric effects to be able to tune the phase over the complete phase interval of $[0;2\pi)$. In this work yet another concept of local phase manipulation is used, which is presented in more detail in the following.

The Pancharatnam-Berry (P-B) metasurface is based on the ability to spatially control the phase of incident light by the polar angle of scatterers of same (anisotropic) geometry at a certain position (x/y) on the surface plane. The local phase shift, known as 'Pancharatnam-Berry phase' or 'geometric phase' [6], that an incident electromagnetic wave gains at the metasurface interface depends linearly on the polar angle of the scatterer, e.g. a gold nanorod, and therefore allows the spatial phase control. The entire phase space range of $[0;2\pi)$ can be covered by the nanorod rotation, which is important to have complete control of the shape of scattered wavefronts. Additionally the polarization of the phase shifted scattered light is converted to opposite helicity during the scattering process. A great advantage of the P-B metasurface is the broadband performance, because of the equal geometry of the scatterers it does not suffer from dispersion. The phase shift is only dependent on the orientation of the scatterer, its sign is dependent on the polarization state of the circularly polarized incident light. A disadvantage is that the complete control over the phase and simultaneously over the polarization of the light is not possible, since the geometric phase is only applied to the polarization converted scattered light [1] and therefore the phase control affects the polarization as well.

The P-B metasurface achieves the phase gradient $\frac{d\phi(x)}{dx}$ to realize the previously introduced anomalous refraction by the spatial variation of the polar angle of the resonators. It was shown that the phase shift difference $d\phi$ of the light gained at the positions of two neighboring resonators of polar angle difference $\Delta\Phi$ is given by [5]

$$d\phi = 2\Delta\Phi. \tag{22}$$

If we assume a metasurface with resonators of constant separation Δx and constant angle difference $\Delta\Phi$ along one surface direction x, a unit cell containing p rods will lead to an angle difference of $\Delta\Phi = \frac{\pi}{p}$ between neighboring resonators. The phase gradient can therefore be expressed by

$$\frac{d\phi(x)}{dx} = \frac{2\Delta\Phi}{\Delta x} = \frac{2\pi}{p\Delta x}. \tag{23}$$

Introducing the unit cell length $L_u = p\Delta x$ and inserting (23) into (21), the total refraction angle of a P-B metasurface with constant phase gradient along one direction of the interface is given by

$$\theta_{\text{tot}} = \arcsin\left(\frac{\lambda_0}{L_u}\right). \tag{24}$$

The angle after the anomalous refraction at the first interface can be simplified with the introduced variables to

$$\theta_r = \arcsin\left(\frac{\lambda_0}{n_r L_u}\right). \tag{25}$$

The law of generalized refraction has been studied in detail and realized with the help of P-B metasurfaces in a previous work of Lingling Huang et al. in 2012. A schematic drawing of their investigation method is presented in figure (6), which shows a metasurfaces made of gold nanorods of a certain angle distribution on a glass substrate, introducing a linear phase gradient in x-direction (a). They use $p = 8$ rods in the unit cell, each at a constant angle difference $\Delta\Phi$ to its neighboring rod, shown in red colour. The different rod configurations, contributing to the unit cell of a metasurface are named 'levels'. The spacing between the rods is equal in both surface directions. The incident circularly polarized light is refracted at the metasurface interface anomalously (b, red), changing its polarization to opposite helicity, traveling through the glass substrate domain to the lower interface, and is refracted there a second time, conventionally, keeping its polarization state. The incident light path, following a conventional refraction at both interfaces is also drawn (b, blue). The use of opposite incident polarization changes the anomalously refracted light path, while the conventional refracted light travels along the same path for both of the incident polarization states (c). The polarization state is described by σ, which refers to a circular polarization of the light, namely either right-handed circularly polarized (RCP) or left-handed circularly polarized (LCP). The polarization state $-\sigma$ refers to the respective opposite helicity, which is then either LCP or RCP, respectively.

This work's single layer metasurface investigation deals with very similarly designed metasurfaces, using normal incident RCP light for simplification.

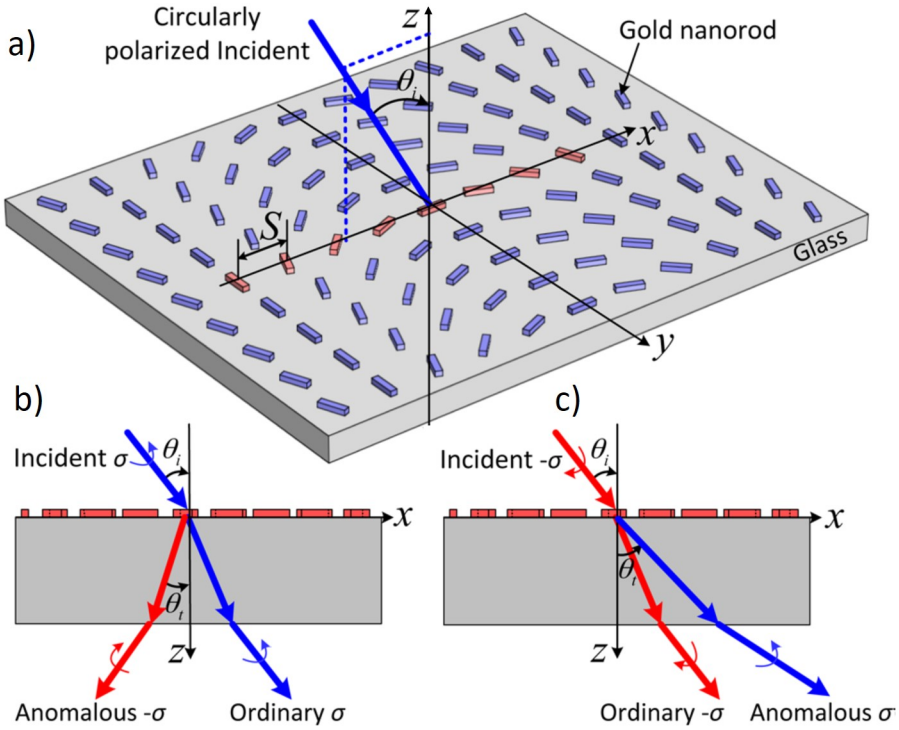

Figure 6: Schematic drawing of a Pancharatnam-Berry metasurface used for anomalous refraction studies (a). The unit cell rods are depicted in red. The spacing between the rods is equal in both surface directions. If circularly polarized light is incident on the metasurface, is is partly refracted anomalously and conventionally at the metasurface interface, followed by a conventional refraction at the lower glass/air interface (b, c). A anomalous refraction process changes the polarization state to opposite helicity, while the conventional refraction does not. Picture taken from reference [11].

The angle of anomalous refracted light depends on the unit cell length L. The fraction of light intensity scattered to this direction, however, was demonstrated to depend on the number of resonators p in the unit cell. To increase the intensity of anomalous refracted light observed at a given, fixed angle, it is possible to increase p while keeping L constant, resulting in the decrease of Δx.

A further question is, why not all of the incident light is refracted anomalously but only a small fraction of it, since we applied the concept of least gathered phase along the path to deduce the generalized refracted equation, which should be the path of all the light then. Within the mathematical deduction of the generalized law of refraction we secretly assumed $\phi(x)$ to be a continuous function of the position x along the interface. For the case of a metasurface, which realizes the spatial phase gradient with the help of local resonators of subwavelength separation, the phase function becomes discrete and shows step-like character. As a result only a fraction of the incident light is refracted anomalously, while the rest undergoes conventional refraction. This limits the metasurface efficiency fundamentally [1]. Another important detail in our treatment of generalized refraction with the help of metasurfaces is that the scattering amplitude of the individual scatterers should be equal and independent from the polar angle, which is necessary for the refracted wave, to be a plane wave again, as assumed in the theoretical derivation. The refracted wave is the superposition of the locally scattered spherical waves, which superimpose to a plane wave only for equal amplitude. The functionality of the P-B metasurface therefore relies strongly on the independence of the scattering amplitude from the polar angle of the individual scatterer, meaning the decoupling of spatial phase and amplitude control for the scattered light by the metasurface.

3 Methods

In the following chapter, the experimental and numerical investigation and fabrication methods are presented. It contains details of the nanofabrication of the samples, experimental measurement methods like scanning electron microscopy and single wavelength optical measurements, as well as simulation methods, which are presented at the end of this chapter.

3.1 Nanofabrication

The metasurface samples investigated are fabricated with electron-beam lithography and subsequent lift-off. This section will provide a detailed description of the fabrication process, starting with spin coating, followed by the lithography process, finally describing the overlay process, which is used to perform a second layer electron-beam lithography step in order to fabricate the double layer metasurfaces. The sample fabrication process completely takes place in a clean room laboratory.

3.1.1 Spin coating process

In preparation of the electron-beam lithography, a thin 'resist' layer is needed on top of the substrate. Therefore a spin coating process is carried out with the 'Easyline EL S 200 BM' spin coater from 'solar semi'. It is used to fabricate layers of the organic electron-beam lithography resist Poly(methyl methacrylate) (PMMA) onto a substrate. A flat glass substrate of dimensions (10×10×0.7) mm, coated with a thin layer of indium tin oxide (15-30) nm is used. Firstly it is cleaned by rinsing with acetone, brushing over its surface with a acetone soaked clean room wipe in two perpendicular directions, rinsing with acetone again, followed by rinsing with isopropanol. Subsequently the clean substrate is dryed with nitrogen and placed on a flat chuck. PMMA solved in chlorobenzene is used. The first layer of PMMA is coated with the parameter set (3000 rpm, 4000 rpm/s, 30 s), wherein the first value corresponds to the spin coating speed, the second value to the acceleration and the last value is the total spin coating time. PMMA of molecular mass of 200 kDa and solid content of 3.5 % is used. A post bake of 5 minutes at 160 °C is carried out on a ceramic hot plate after the back side of the sample is cleaned with acetone by rubbing it over a acetone soaked wipe on top of an edge. The layer thickness is repeatedly checked for control samples and

evaluated to (160 ± 10) nm with a profilometer ('DektakXT' from 'Bruker'). The second PMMA layer is coated with a parameter set of (6000 rpm, 4000 rpm/s, 30 s), using a PMMA of molecular mass of 950 kDa and solid content of 1.5 %. Again the back side cleaning and a post bake of same time and temperature is performed. The total PMMA layer thickness is repeatedly checked to be (220 ± 14) nm. A sufficient time is waited between coating the first and second layer to cool down the sample to room temperature again after the first baking process, to make sure both spinning processes are performed at room temperature. The spin coating process completely takes place under ambient conditions.

3.1.2 Electron-beam lithography

The electron-beam lithography (EBL) process is carried out with the 'eLINE Plus' tool from 'Raith'. The essential steps of the standard lithography process are summarized in figure (7). First a PMMA resist layer is spin coated onto a glass substrate as described in the previous section (a), followed by the electron-beam exposure of the desired pattern (b). In a development step the exposed parts of the PMMA resist layer are dissolved (c), leaving a patterned PMMA resist layer behind. A gold layer is evaporated on top (d), sticking to the PMMA layer as well as the revealed substrate surface parts. In a final lift-off step (e), the residual PMMA layer together with the residual gold on top is dissolved, resulting in the desired gold pattern on the substrate. A more detailed description of the different steps is given in the paragraphs below.

Pattern design The design consists of a 500×500 μm square field, divided into 5×5 write-fields of 100×100 μm size. The outer rim of write-fields in this array contains the markers. The 4 write-fields at the corners contain large global marker crosses, the outer left row of write-fields contains small marker crosses. Within a overlay process, the global marker crosses are needed for a 3-point pre-alignment, the small crosses are used for the write-field alignment. The metasurface nanorod pattern is contained by the inner square of 3×3 write-fields and therefore has a size of 300×300 μm^2. The design is shown in figure (8).

Writing process The spin coated substrate is loaded into the EBL and driven upwards until a working distance of 9.8 mm is reached. The EHT (net

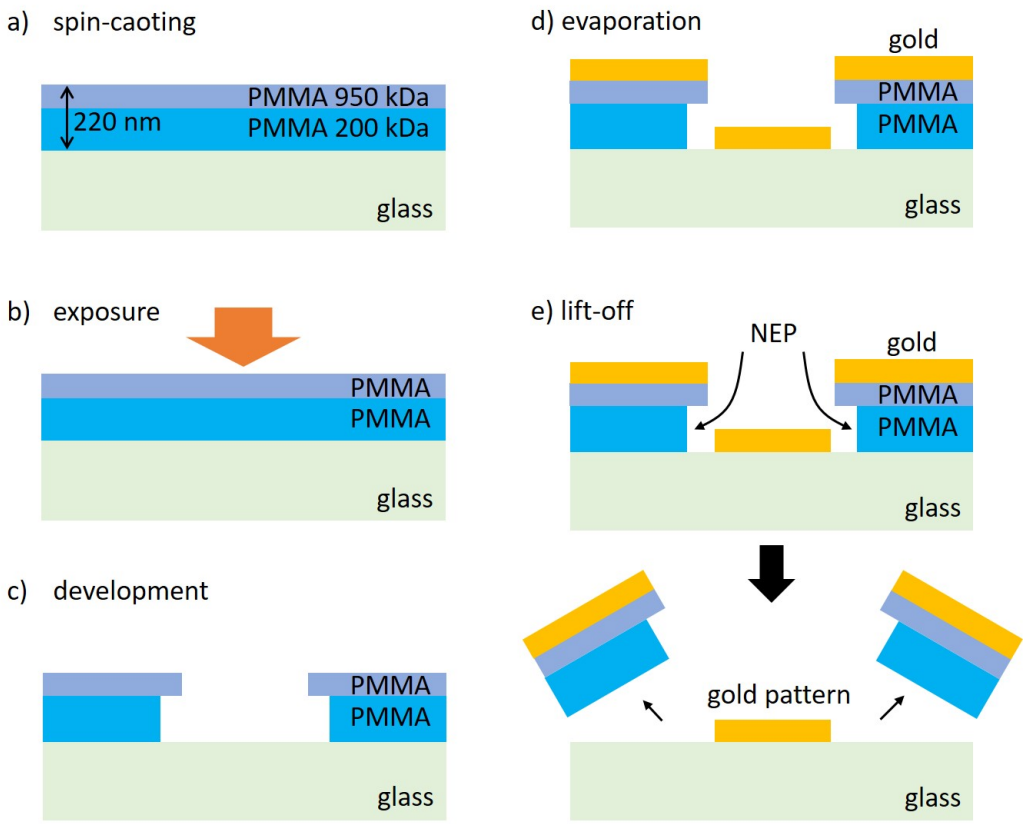

Figure 7: Step-by-step overview of an electron-beam lithography process, using a double-layer PMMA resist. The glass substrate is depicted in green, the PMMA resist layers in blue and the evaporated gold layer in yellow. The chemical used to dissolve the PMMA layer in the lift-off step (e) is N-Ethyl-2-pyrrolidon (NEP).

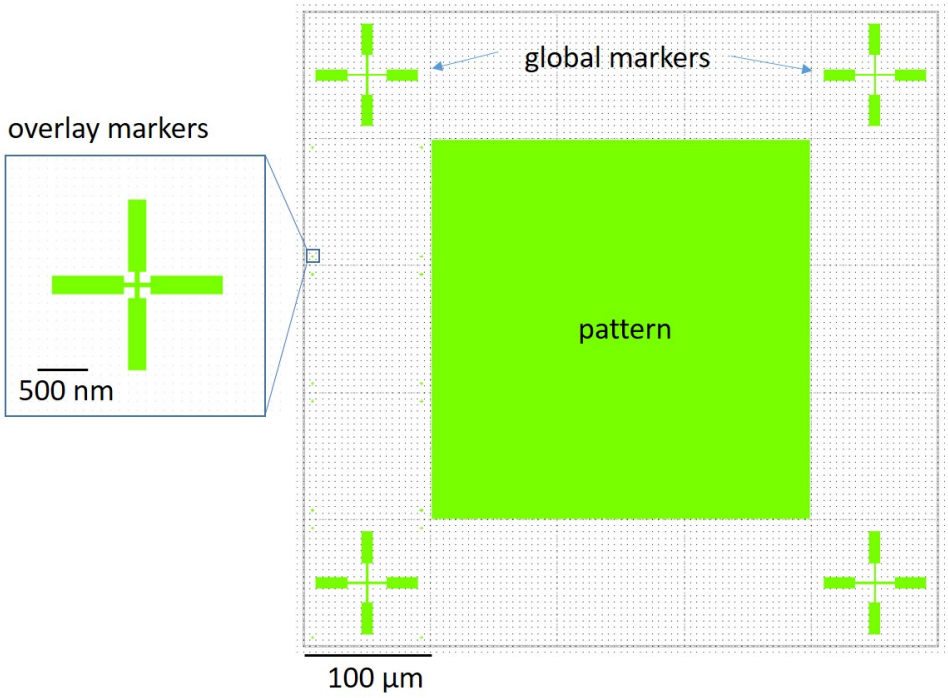

Figure 8: GDSII-layout of the metasurface pattern. The total area is divided into 25 quadratic write-fields of 100 μm length. The actual metasurface pattern, the global markers and the small overlay makers (enlarged inset) are shown.

acceleration voltage) is set to 20 kV, the aperture to 10 μm. Subsequently the beam current is measured at the faraday cup of the sample holder. The 'dynamic compensation' is switched off and the writing mode is set to 'meander mode'. A dose of 300 $\mu C/m^2$ is used with a dose factor of 0.9. The basic step size is 2 nm and the step size 6 nm. A write-field of 100×100 μm^2 is used.
The sample-coordinate system (U, V) is adjusted by performing an origin and angle correction with the help of the lower left and lower right corners of the sample. The aperture and stigmatation adjustment is performed on a dust particle of micrometer dimensions and subsequently on a burned contamination carbon dot for a magnification of 300k or more. A manual write-field alignment is performed. The write-field alignment procedure corrects and matches the coordinate systems of the beam and the stage. Only if there is a good degree of matching, the different neighboring write-fields fit in angle, size and shift, which is important for the quality of a pattern of larger extension than one write-field, which is the case for the metasurface pattern in this work.
After driving to the desired patterning position on the sample, a 2×2 carbon dot matrix is created, the stigmatation and aperture adjustment is corrected a second time, such that the dots are circularly shaped with a diameter of 20 nm. Afterwards, an automatic write-field alignment with images is performed 2-3 times. After reaching the desired alignment accuracy (variation of shift, rotation and zoom factor only within the last digit), the exposure is started.

Development process The electron-beam exposes the PMMA resist layer with the designed pattern and dose. The energy deposition cracks the polymer chains of the PMMA and reduces its molecular mass at the exposed areas. In a further development step, the sample is put into an organic solvent which dissolves only the reduced molecular mass polymer chains of the PMMA layer, resulting in a negative pattern transfer. The PMMA resist layer then contains 'holes' which reveal the underlying substrate surface at the exposed areas. Such a resist is called 'positive' resist.
For the development process, two beaker glasses are prepared, one filled with the organic solvent dilution Methyl isobutyl ketone (MIBK) 3:1 isopropanol, the other one with isopropanol only. The exposed sample is unloaded and put into the diluted MIBK beaker for 90 seconds without moving the sample

within the beaker. Immediately after, the sample is put into the isopropanol beaker for 60 seconds and afterwards dried with nitrogen (low pressure). The exposed pattern is now transferred into the PMMA layer.
A two layer PMMA resist is used to create undercuts at the walls of the trenches after the developing step. The resist layers of different molecular masses are dissolved on individual time scales. The 950 kDa PMMA layer is dissolved slower than the underlying 200 kDa PMMA layer. The resulting undercut structures are beneficial for the lift-off process (compare figure (7e)).

Evaporation process A gold layer is evaporated on top of the sample. After the evaporation step, the gold layer is on top of the PMMA, as well as directly on the substrate at the developed areas. The pattern is therefore transferred into a positive gold pattern on the substrate.
The evaporation process is performed with the electron-beam evaporator 'WINTER HVB 130'. The sample is rotated at a speed of 20 rounds per minute during the evaporation. A adhesion layer of 2.5 nm of chromium is evaporated, followed by a evaporation of 40 nm of gold. In general it is recommended that the maximum metal layer thickness should not exceed a quarter of the resist layer thickness in order to optimize the upcoming lift-off step. This is fulfilled for the given fabrication parameters.

Lift-off process To reveal the gold pattern, the residual PMMA layer, together with the residual gold on top, has to be removed in a lift-off step. In order to dissolve the PMMA layer, the organic solvent N-Ethyl-2-pyrrolidon (NEP) is used. The undercut structures are very helpful to increase the contact of the NEP and the PMMA. Otherwise the PMMA layer would be covered completely by the gold layer and protect it from the NEP.
For the lift-off, the sample is put into a beaker filled with NEP and heated up to 55 °C in a heat bath for 4 hours without sonication. A syringe with acetone is prepared to rinse away the desorbed residual PMMA layer together with the residual gold on top. This rinsing step is performed while the sample breaks through the NEP fluid surface under a steep angle. The sample is dried with nitrogen afterwards. The fabrication process of the first layer pattern is finished and checked by SEM. The described fabrication process is used for the single layer metasurfaces reported in this work. For the double layer metasurface stack, a second EBL-step has to be carried out, which is

called 'overlay-process'.

Overlay process The fabrication of another gold pattern on top of the first one is possible by using a second EBL-step. A step-by-step illustration is given in figure (9). The fabricated single layer sample is spin coated with a 70 nm thick spacer layer of PC403, a spacer polymer used for planarization. After a baking process of 30 minutes at 180 °C, the PC403 layer is stable against acetone, isopropanol, NEP and MIBK and has a refractive index value of approximately 1.5, very similar to that of glass. In addition the surface of the PC403 layer has a very small roughness, which is shown to be remarkably independent of the shape and size of underlying structures, making it a perfect candidate for the spacer layer, since this layer is the new 'substrate' for the second EBL-step and has to be stable against the upcoming development and lift-off process.
The PMMA layer is spin-coated on top of the PC403 layer as described in the previous section (a). The EBL-parameters stay the same as well. A 3-point alignment is performed to adjust the second exposure to the previous pattern. Therefore the large marker crosses in the corner of the existing pattern are used. During the exposure the machine will execute a manual write-field alignment at the first write-field of each row of write-fields. This will increase the alignment accuracy and alignment isotropy of the two patterns.
After the development, evaporation and lift-off step (b, c and d), performed as described priviously, the fabrication of the stacked nanostructure pattern is finished. All double layer metasurface stacks reported in this work are fabricated following this procedure.

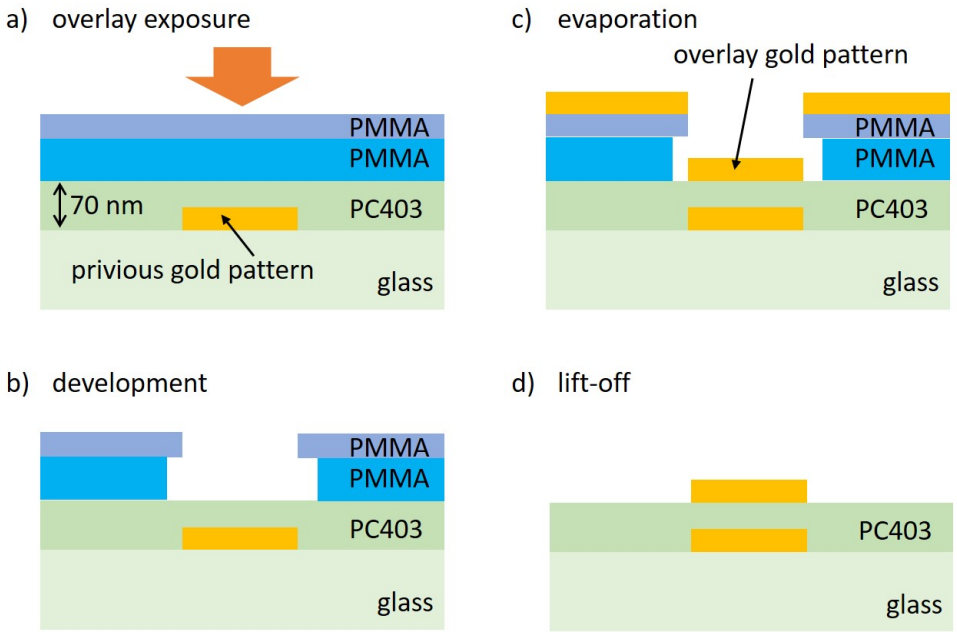

Figure 9: Step-by-step overview of an overlay electron-beam lithography process. The previously patterned substrate is coated with a spacer layer of PC403 (green) and the double layer PMMA resist (blue) and exposed a second time with the desired overlay pattern (a). The PC403 layer is stable against the upcoming development step (b). The evaporation of the gold layer is shown in (c). The PC403 layer is as well stable against the final lift-off step (d).

3.2 Scanning electron microscopy

The scanning electron microscopy images are produced with the 'eLINE Plus' tool from 'Raith'. The rod length error is estimated to $\Delta L = \pm 10$ nm. The alignment error of the stacked metasurfaces is evaluated to also ± 10 nm. The error of the width and periodicity is neglected, as it has no important impact and is not topic of discussion in this work.
A EHT of 20 kV, a aperture of 10 μm and a working distance of 9.8 mm is used, such that the parameters of the writing process agree with the parameters of the investigation process. The magnification for the images shown in this work is 15k and 30k. The 'InLens' detector is used. It is a ring-shaped secondary electron detector, located right above the objective within the lower end of the electron acceleration column. The ring configuration in combination with the short distance to the sample provides shadow-free imaging with high resolution even for lower acceleration voltages.

3.3 Optical measurements

The fabricated single and double layer metasurfaces' performance is measured with the help of an optical single wavelength setup. In this section the experimental setup is described and explained, followed by a detailed introduction to the measurement process itself. The quantities of interest is the power of anomalously refracted light as well as the refraction angle itself. Therefore a setup is constructed, capable of measuring the transmitted power for an angle interval of (-45 to +45)° behind the sample.

3.3.1 Experimental setup

The setup, schematically shown in figure (10), is used to measure the angle resolved power of transmitted monochromatic light at normal incidence on the sample. The setup contains a 30 mW laser diode, which emmitts monochromatic light at a wavelength of 980 nm. The divergent light is collimated by a collimation lens. After passing a linear polarizer (LP 1, wavelength range (550 - 1500) nm, transmission efficiency 82%, extinction ratio 10^8), followed by a quarter wave plate (QWP 1, retardance accuracy at operational wavelength 3 nm, reflectance 0.25%), which fast axis includes a 45° angle difference with the polarization axis of the linear polarizer, the light is circularly polarized. Subsequently, an aperture is used to achieve a circular

beam profile and a submillimeter beam diameter (not shown in the figure). The light hits the sample at normal incidence, passes through a quarter wave plate (QWP 2, same specifications) and a linear polarizer (LP 2, same specifications) again, and finally gets detected by a silicon photo diode with an active detector area of 9.7 mm × 9.7 mm, a wavelength detection range of (400 - 1100) nm, a power range of 50 nW - 50 mW, a power resolution of 1 nW and a measurement uncertainty of ±3% for the used wavelength. These last three optical components behind the sample are collectively mounted onto a rotatable arm, which allows the rotation of the optical axis behind the sample in a half-circle around the sample. The center of this half-circle is located exactly underneath the nanostructured area of the sample. The laser diode and the sample are mounted onto a xyz-stage which micrometer resolution and the ability to adjust the polar angle. Additionally a 20×-objective is used to check that the beam hits the nanostructured area of the sample, but is removed during the actual measurement process and therefore not shown in the setup illustration.

3.3.2 Single wavelength measurements

Polarization selective measurements at a wavelength of $\lambda_0 = 980$ nm have been carried out for various metasurface samples. Therefore both linear polarizers are oriented at the same angle in respect to their polarization axis. Also both the fast axis' of the QWPs are oriented at the same angles, which include a angle difference of 45° to the polarization axis' of the linear polarizers. For this configuration, only the polarization converted light is able to pass the second linear polarizer, since the polarization axis of the transmitted light is rotated back to the initial state after the second QWP only for the opposite handedness. Thus, the anomalous refracted and polarization converted light is detected, while the conventional refracted or transmitted light is filtered. This is schematically presented in figure (11). The collected data for the power is the mean of a measurement process over 30 seconds, while taking one data point every second. The error is identified with the standard deviation. The angle value can be adjusted with the help of the rotation platform, upon which the arm with the second QWP, LP and detector is located. The error of the angle is influenced by the ratio of the detector surface diameter and its distance from the sample, the degree of alignment of the rotation axis and the sample plane, as well as the accuracy of the angle scale bar itself. It is estimated to $\Delta\Theta_{\text{tot}} = \pm 1.5°$.

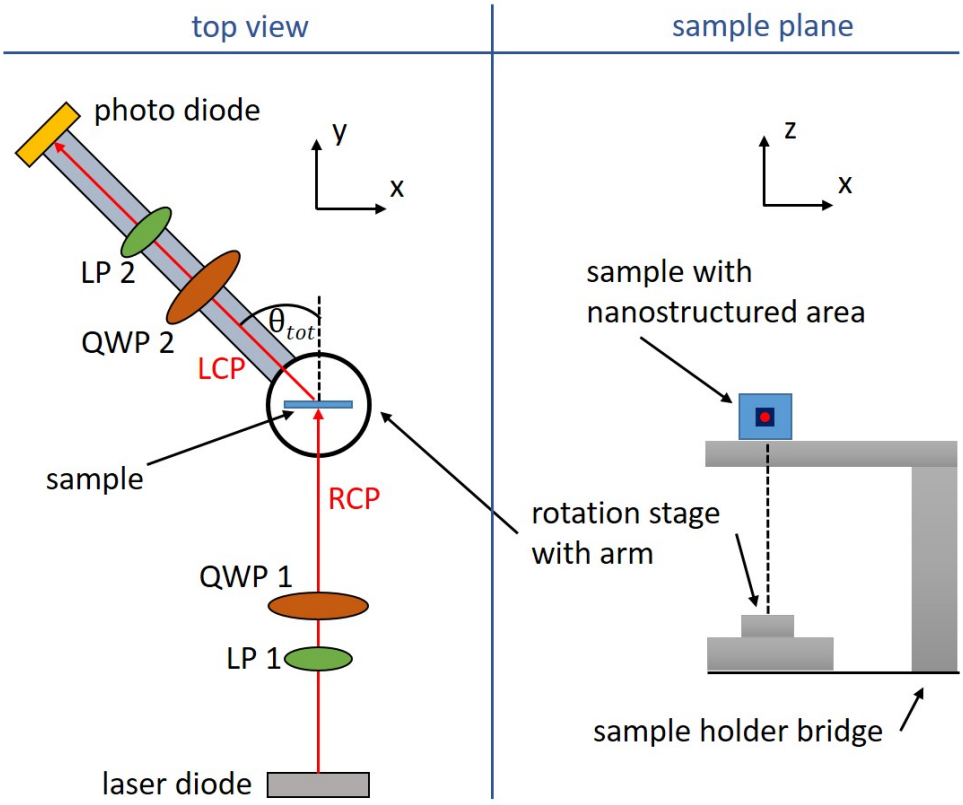

Figure 10: Schematic presentation of the experimental setup used for angle resolved, polarization selective power measurements of transmitted light of the metasurface samples. The top view is given on the left hand side, while a vertical cut through the sample plane is shown on the right hand side. The light is indicated by red arrows. It is emmitted by a laser diode (grey), passes a linear polarizers (LP 1, green), a quarter wave plate (QWP 1, brown), incides at the sample (blue) at normal incidence and is refracted according to the metasurface design at an angle Θ_{tot} measured against the sample surface normal. Thereafter, the refracted light passes the QWP 2 and LP 2 and is finally detected by a photo diode (yellow), measuring the incident power. The optical components behind the sample plane are mounted on a rotatable arm with the center of rotation lying directly underneath the nanostructured area of the sample.

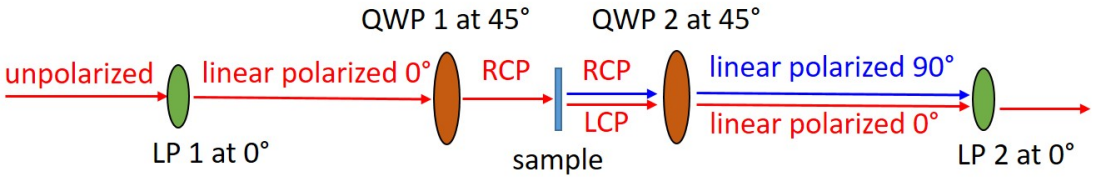

Figure 11: Schematic presentation of the polarization filtering of the experimental optical setup. The light incidence is indicated by red arrows. After passing the LP 1 the unpolarized light is linearly polarized. The following QWP 1 leads to right-handed polarized light (RCP), which incides on the sample at normal incidence. Thereafter, partly RCP and partly LCP light is found, of which the LCP was anomalous refracted and the RCP conventionally. The QWP 2 retards the two polarization states differently, since the electric field vector rotates in opposite directions. The result is perpendicular states of linearly polarized light, of which only the previous LCP can pass the final LP 2.

3.4 Simulations

The simulations presented in this work are carried out with the software 'COMSOL Multiphysics'. The 'RF-module' is used for the finite element calculation method within the frequency domain.
The setup for the simulations of the conversion efficiency and phase shift of the gold rod arrays is realized by a unit cell containing two blocks of square base with the length P and height of 1000 nm, exactly stacked on top of each other. The refractive index of the upper block and lower block is $n = 1$ and $n = 1.45$, respectively, representing the air and substrate domain. The surfaces shared by the blocks is the top surface of the substrate. Periodic boundary conditions for the electromagnetic fields is imposed for each pair of opposing vertical surfaces. The gold rod is modeled by another block of dimensions L, W and a height of 40 nm, with its center point lying 20 nm above the center point of the square base of the air block. The dielectric function of gold, taken from [7], is imposed on this domain. The gold domain is modeled with a electric conductivity of 0 and a magnetic permeability of 1. A block of 200 nm height is used underneath the substrate block as a perfectly matching layer, modeling the substrate block as a half-space, preventing any reflection from the bottom surface. In addition a fillet of 10 nm radius is used to round the corners of the top surface of the gold domain, keeping

the simulations closer to real structures. The gold rod domains are meshed with a maximum element size of 10 nm, the air and substrate domain with a maximum mesh size of 80 nm. The 2 nm chromium adhesion layer as well as the 15-30 nm indium tin oxide layer on the substrate is neglected and not taken into account in the simulation setup. This setup is used for the single layer gold nanorod array simulations in this work.
For the simulations of the stacked gold nanorod arrays the setup is modified by an additional gold block, vertically shifted downwards by S into the substrate domain, representing the lower layer of the stacked gold rod array configuration. Both the polar angles of the two gold blocks can be modeled individually.
For the simulations of the metasurface, a 8 level unit cell is designed by extending the surrounding-domain blocks in x-direction by a factor of 8 and adding the mising nanorod blocks with their individual polar angles.
For the simulations of the magnesium and magnesium hydrid metasurface unit cells, the corresponding domains are modeled by the materials' dielectric functions, taken from [7], again with a electric conductivity of 0 and a magnetic permeability of 1.
A 3D and a top view of both, the setup for simulating the nanorod arrays as well as the metasurfaces, is given in figure (12). The single layer simulations only use the rods depicted in blue. The double layer simulations additionally use the lower layer rods shown in transparent grey.

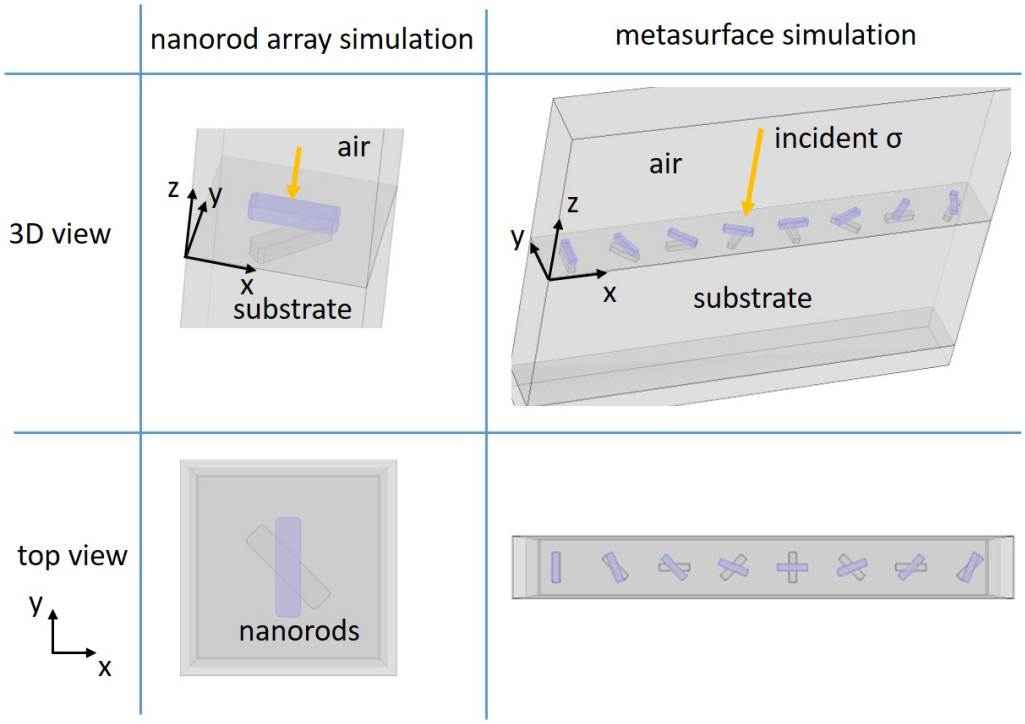

Figure 12: Illustration of the unit cells for the simulations of the nanorod arrays as well as the metasurfaces in 3D view and top view. For the single layer simulations only the blue rods are used, for the double layer the underlying transparent grey rods are used in addition. The CPL light at normal incidence coming from the air block is indicated by the yellow arrow. An example for a relative rod angle of 45° (array simulations, left) and for a double layer metasuface stack containing a metasurface of angle difference 22.5° on top of one with angle difference 45° (right). Note that the air and substrate domain is not shown to full extend.

For all simulation setups, the incident planar wave's electric field is incident from the top surface of the air block with an amplitude of

$$\vec{E}_0 = \begin{pmatrix} 1 \\ i \\ 0 \end{pmatrix} \tag{26}$$

and wave vector of

$$\vec{k}_0 = \begin{pmatrix} 0 \\ 0 \\ -k_0 \end{pmatrix}, \tag{27}$$

corresponding to RCP light, where $k_0 = \frac{2\pi}{\lambda_0} > 0$.

4 Results and Discussion

In the beginning of this chapter the simulation and experimental results for two different single layer metasurfaces are presented. Subsequently the results of the simulations and optical experiments on combinations of these two single layer metasurfaces within a double layer stack is discussed. Thereafter, a concept of further modification of the metasurface stack is explained, implementing the ability of post-fabrication dynamic steering of light beams. An overview of the objective of this chapter is presented in figure (13).

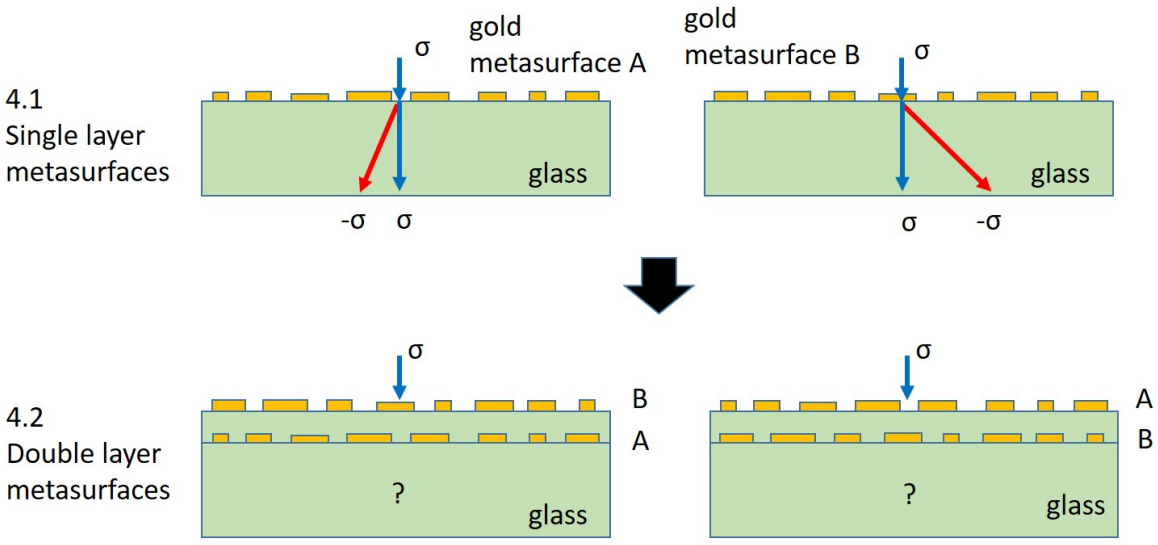

Figure 13: Overview of the work flow of this chapter. First two single layer gold metasurfaces A and B are investigated. Thereafter, they are combined into a metasurface stack and the two possible configurations (A/B) and (B/A) are investigated.

4.1 Single layer metasurface

The first section presents single layer metasurfaces, realizing the anomalous refraction in order to deflect an normal incident light beam into a given direction. Two differently designed metasurfaces for two distinguishable refraction directions are reported, investigated by simulation and experiment, and finally discussed. In the beginning, simulations of gold nanorod arrays are presented, which provide insight in the general working principle of a metasurface. Subsequently, the transition form the study of these arrays to the actual metasurface design, realizing the anomalous refraction, is explained.

4.1.1 Pancharatnam-Berry phase shift and conversion efficiency of gold nanorod array

The purpose of a metasurface is the spatial control of certain properties of incident light by the nanostructure design on top of the surface. In order to understand how the phase of incident light depends on the shape and position of the nanostructures, simulations of gold nanorod arrays on top of a glass surface have been carried out. The simulation setup is shown in figure (14). The normally incident light is circularly polarized and incides on the surface from an air half-space from top. The rods of dimensions length $L = 200$ nm, width $W = 50$ nm and height $H = 40$ nm, have a periodicity of $P = 400$ nm along both surface directions and are collectively oriented at a polar angle Φ.

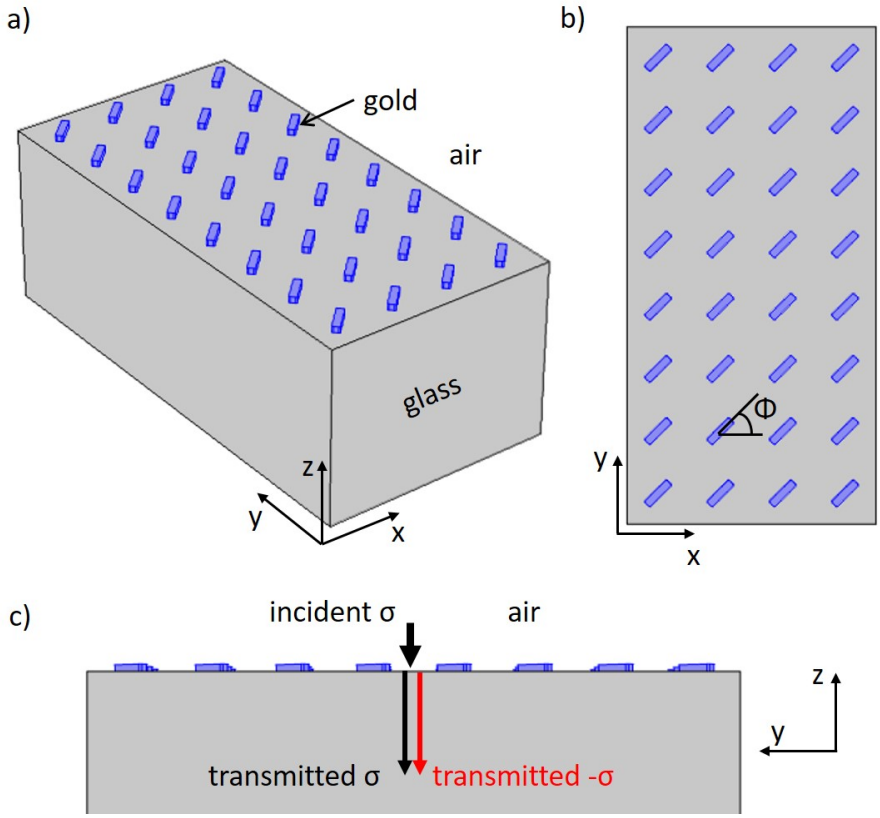

Figure 14: Schematic drawing of a gold nanorod array on top of a glass substrate surrounded by air, in 3-dimensional view (a), top view (b) and side view (c). The collective orientation of the gold rods (blue) are described by the polar angle Φ. Normal incident light of polarization σ (black arrow) is transmitted into the glass space, partly changing its polarization (red arrow) by resonant scattering at the gold rods.

The array is simulated for different polar angles Φ in steps of $\Delta\Phi = \pi/8 = 22.5°$. The incident polarization state is denoted σ, which can be either RCP or LCP. The polarization converted light in respect to the incident light is named $-\sigma$. It is known that only the polarization converted light gathers the P-B phase, which will be used to construct the metasurface phase gradient at the end. Therefore the quantity of interest is the polarization conversion efficiency of the nanorod arrays, corresponding to various rod angles, and their phase shift on the polarization converted light.

Polarization conversion efficiency The polarization conversion efficiency is defined as the intensity $I_{-\sigma}$ of transmitted $-\sigma$ polarized light divided by the total intensity I_σ of incident (σ polarized) light,

$$\text{conversion efficiency} = \frac{I_{\text{transmitted}}(-\sigma)}{I_{\text{incident}}(\sigma)}. \tag{28}$$

The polarization conversion efficiency spectra are shown in figure (15). The best conversion efficiency can be achieved for wavelengths, which match the resonance position of the plasmonic resonance of the gold rods, because this resonant scattering process is responsible for the polarization conversion and the applied P-B phase.
The spectral position of the plasmonic resonance is dependent on the aspect ratio AR $= L/W$ of the rods, according to equation 3. For the simulated dimensions ($L/W = 4$) the maximum polarization conversion appears to be at $\lambda_{\text{max}} = 930$ nm. There is no dependence of the conversion efficiency on the rod angle.

Phase shift The phase shift of the incident light $\Delta\phi$ gained at the interface by the resonant scattering process is evaluated for a fixed wavelength of $\lambda_{\text{max}} = 930$ nm for the different rod angle positions and depicted in figure (16). The phase shift depends linearly on the rod angle (compare equation 22) and furthermore covers the complete phase interval $I_\phi = [0; 2\pi)$, meaning the two important working principles for the P-B metasurface are fulfilled. It should be noted, that the phase profile is also checked for various other off-resonant wavelengths, giving the same phase shift results, because of the broadband independence of the conversion efficiency on the rod angle. Thus, the working principles are still fulfilled for other wavelengths, merely the conversion efficiency overall is lower, depending on the degree of off-resonance.

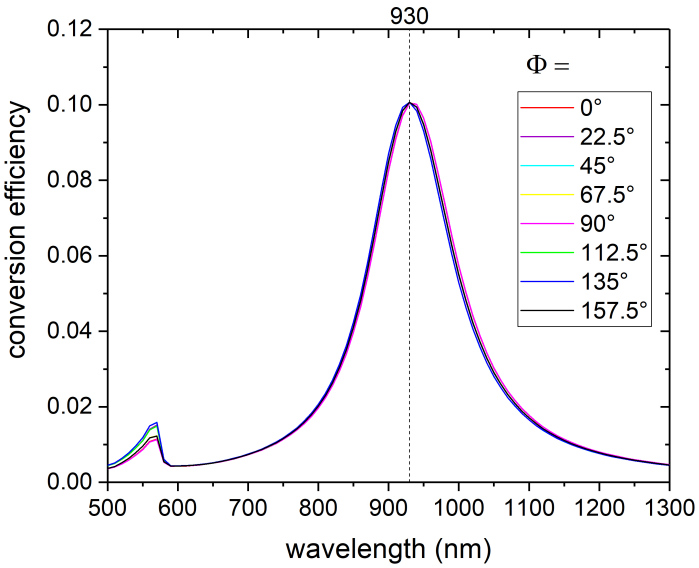

Figure 15: Simulated polarization conversion efficiency spectra for different rod angles Φ in the visible and near-infrared wavelength range. The dashed line represents the wavelength $\lambda_{\max} = 930$ nm of maximal conversion efficiency. The inset shows the independence of the conversion efficiency for this wavelength on the rod angle Φ.

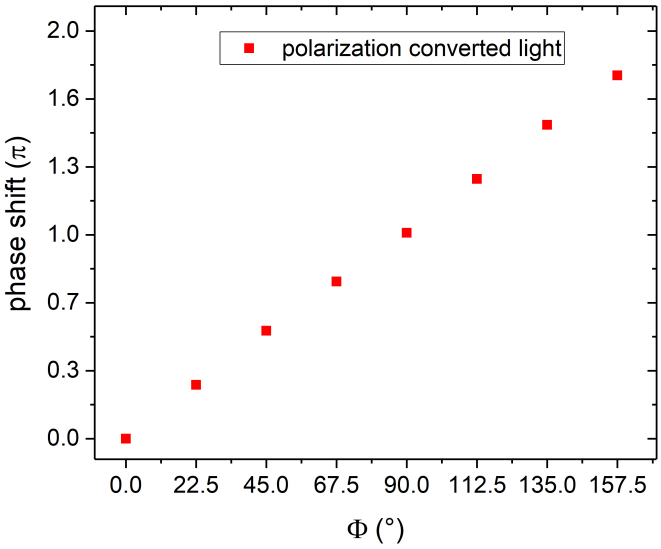

Figure 16: Simulation results of the phase shift dependence, which the transmitted polarization converted light gains at surface of the nanorod array, on the orientation angle Φ of the rods.

Refractive index At the end of this section the influence of the refractive index is investigated by simulations. Therefore the conversion efficiency spectrum of a gold rod array on top of a glass substrate, where the rods are surrounded by air, is compared to the spectrum of an array which is embedded in a medium with refractive index of n = 1.45. The results are shown in figure (17). This configuration is experimentally realized later in this work by coating an additional polymer layer with corresponding refractive index on top of the nanostructured substrate. The increase in refractive index is observed as a red shift of the LSPR-peak. For a incident wavelength, which corresponds to the peak maximum for the air-embedded configuration, a significant drop of conversion efficiency for the polymer-coated configuration is predicted, since the peak maximum shifts away and the conversion efficiency value on the peak flank is far smaller than for the peak maximum.

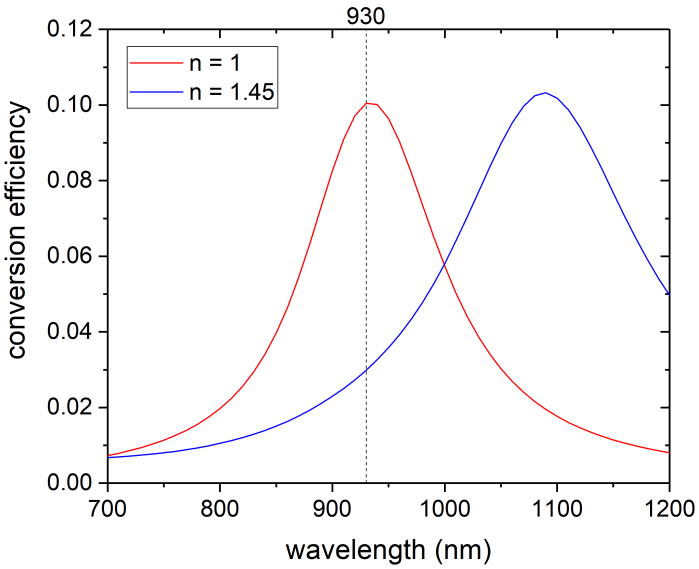

Figure 17: Simulated conversion efficiency spectra for gold nanorod arrays within different refractive index environment. The nanorods embedded in air are shown in red. The blue spectrum is received by simulating an additional layer on top of the rods of 70 nm thickness, embedding them into an environment of refractive index 1.45. A red shift of the resonance is observed.

4.1.2 Metasurface for anomalous refraction

A metasurface is designed in the following, using a unit cell of gold rods spaced at same distance on top of a glass substrate, oriented in the previously discussed 8 different angle positions (called 'levels' in the following), to introduce a linear phase gradient along the x-axis of the surface. Two different metasurfaces are under investigation, both corresponding to different unit cell lengths L_u. The schemes of the two metasurface unit cells are presented in figure (18).

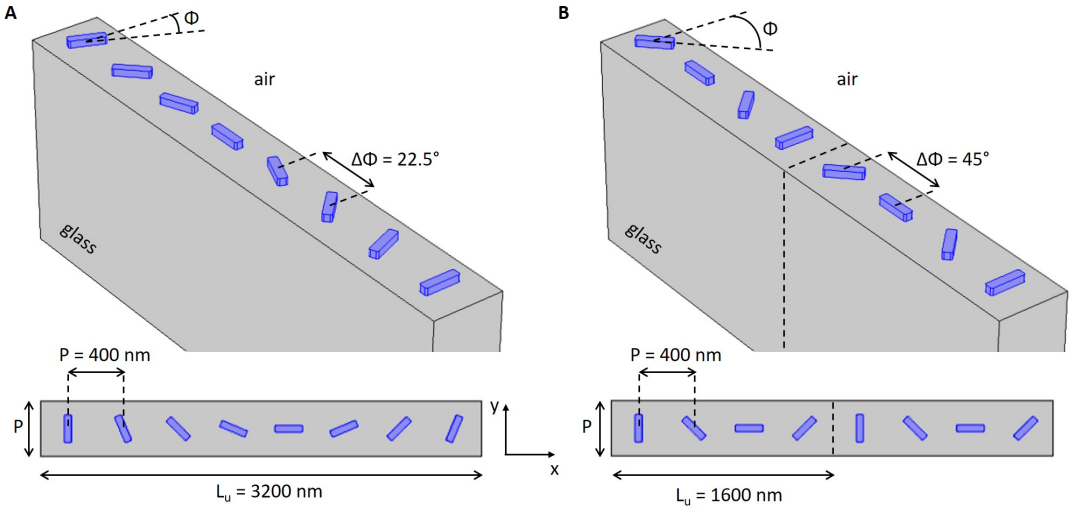

Figure 18: Schematic illustration of the unit cells of two PB-metasurface with different linear phase gradients along the x-direction in 3-dimensional view (top) and top view (bottom). For constant periodicity P between the neighboring rods for both metasurfaces along both surface directions x and y, a smaller angle difference $\Delta\Phi$ leads to larger unit cell length L_u. For a doubled angle difference between neighboring rods along the x-direction, the unit cell length of metasurface B is half of that of metasurface A, which is illustrated by the dashed lines.

The simulation of the two metasurfaces A and B, corresponding to different unit cell lengths, are shown in figure (19). The normalized electrical field in the xz-plane is depicted for both polarizations of transmitted light. The normal incident light is circularly polarized with a wavelength of $\lambda = 930$ nm. The dashed lines show a 0°, 12° and 24° reference line in respect to the x-axis. The black arrow represents the wave vector $\vec{k}$ of the transmitted plane light wave.

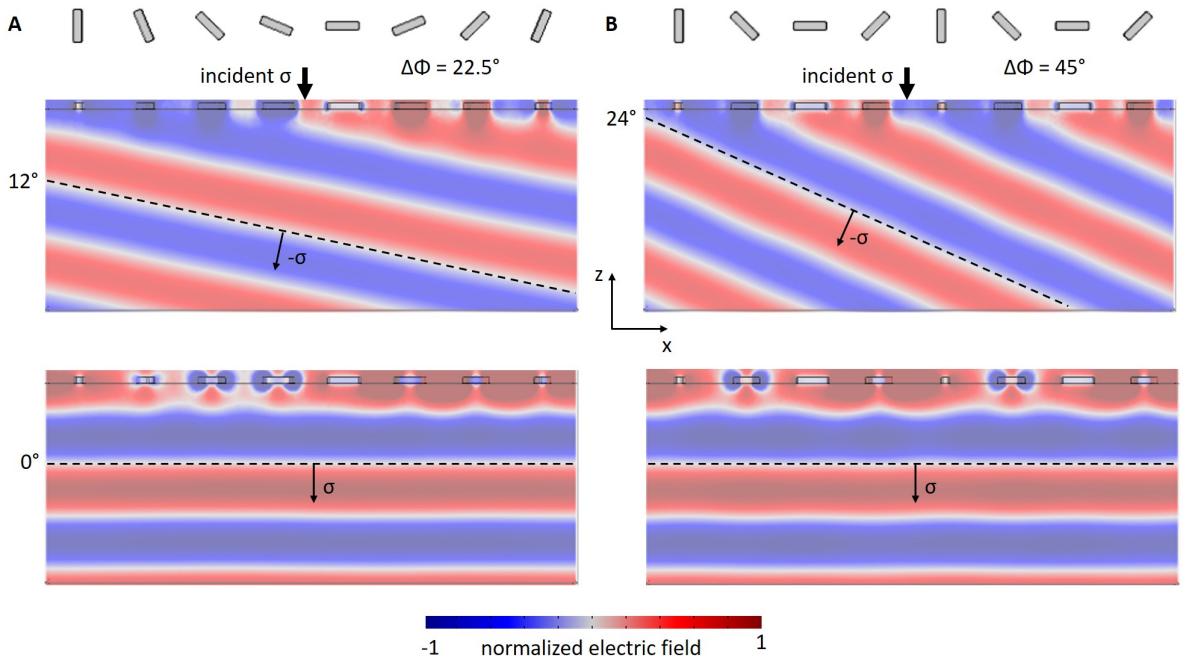

Figure 19: Simulated transmitted electric field for the metasurface A and B for converted polarization (top) and unconverted polarization (bottom) in a side view perspective of the glass half-space. The black arrows represent the direction of the wave vector of the light wave. The anomalous refraction can be observed for the polarization converted light only (top). The angle of anomalous refraction depends on the unit cell length of the metasurface. The dashed lines represent 0°, 12° and 24° reference lines.

The theoretical predictions for the anomalous refraction angle for the metasurface A, corresponding to the unit cell length $L_A = 3200$ nm, is

$$\theta_A = \arcsin\left(\frac{\lambda_0}{n_{\text{glass}} L_A}\right) = 11.6°, \tag{29}$$

and for metasurface B with $L_b = 1600$ nm, it is calculated to

$$\theta_B = \arcsin\left(\frac{\lambda_0}{n_{\text{glass}} L_B}\right) = 23.6°, \tag{30}$$

according to equation 25. The conventional refracted light just passes through the surface without refraction and polarization conversion, due to the normal incidence of incoming light. The simulated results agree very well with the analytical calculations and predictions.
The previously studied independence of the conversion efficiency from the rod angle means a decoupling of scattered intensity of the polarization converted, at each level locally scattered light, and its phase shift. This is a very important working principle of the metasurface, because the locally scattered (and phase shifted) spherical waves superimpose to planar wave fronts only for equal intensities.
The SEM-images of the experimental realization of metasurface A and B is shown in figure (20). The unit cells contain 8 and 4 levels, respectively.

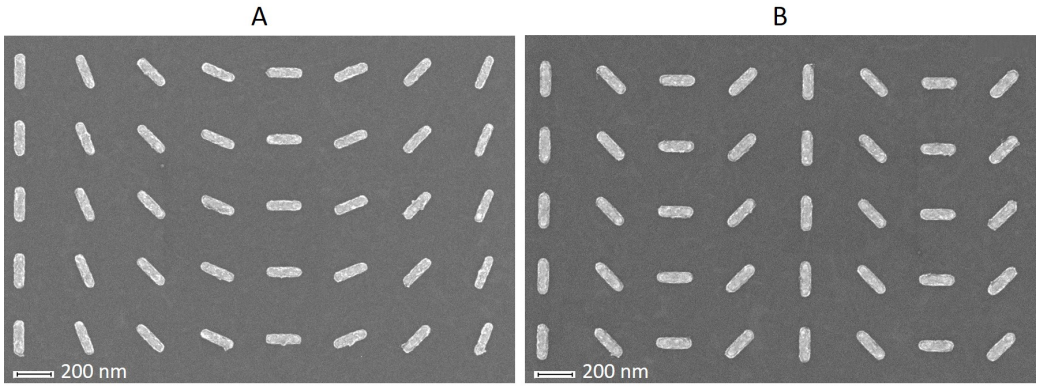

Figure 20: SEM-image of metasurface A and B. The gold rods are shown in white. The unit cell contains 8 levels for A and 4 levels for B.

Single wavelength measurements have been carried out for a wavelength of $\lambda_0 = 980$ nm. The angle dependent power is detected with a photo diode. The setup is described in detail in the previous chapter 3.3. The results are plotted in figure (21). Both metasurfaces A and B are plotted within this graph for ease of comparison, even though they are measured one after another. The power peaks corresponding to the metasurfaces are named with A and B. The metasurface stack is depicted as well, indicating the light direction by a yellow arrow. The grey part indicates the initial medium, which is air for the measurement points in red and PC403 for the blue measurement points.
The theoretical predictions for the total refraction angle of anomalous refracted light for the two metasurfaces are

$$\theta_{\mathrm{A,\ tot}} = \arcsin\left(\frac{\lambda_0}{L_A}\right) = 17.8^\circ \tag{31}$$

and

$$\theta_{\mathrm{B,\ tot}} = \arcsin\left(\frac{\lambda_0}{L_B}\right) = 37.8^\circ, \tag{32}$$

and marked by dashed vertical lines at the corresponding position within the graphs. The 0° measurement point is left out, as the intensity outreaches the power value range on the y-axis. The incident laser power is $P_0 = 100$ μW, resulting in an efficiency of 1.6 % for both of the single layer metasurfaces measured in this work. The background power is about 25 nW, resulting in a signal-to-noise ratio of 65. The experimentally detected anomalous refraction angles agree very well with the theoretical predictions of the generalized law of refraction. Also they are predicted to be independent from the initial medium for normal incidence, which is observed in this experiment as well.
It should be noted that the simulated metasurface refraction angle values and the measured angle values can not be compared directly, as the simulations just show the transmitted light within the glass half-space, while the experimental results show the total refraction angle, measured after the light undergoes a second (conventional) refraction at the glass/air interface before reaching the detector. The wavelengths used in the simulation and in the experiment differ slightly as well, since the experimentally available wavelength is not exactly 930 nm for this work, but 980 nm. To get an impression on

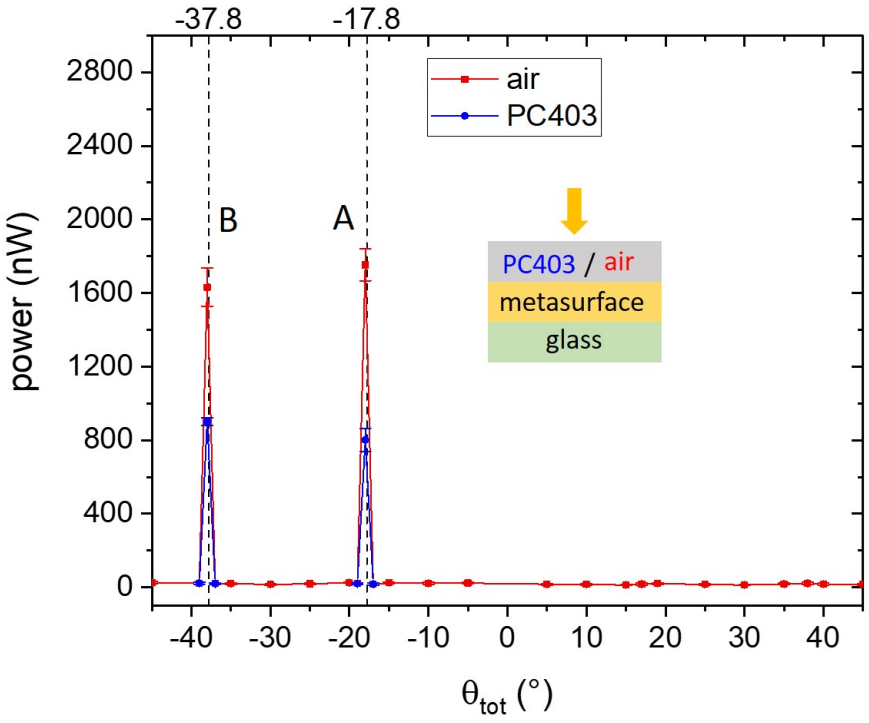

Figure 21: Graph of the angle resolved power measurements of metasurface A and B within one graph for the ease of comparison. Each metasurface is measured one after another. The layer stack is shown, indicating the light direction and the initial medium. The red profile belongs to measurements with initial medium air, the blue to measurements for initial medium PC403. The PC403 medium is realized by an additional layer, spin coated on top of the metasurface. The dashed lines indicate the calculated refraction angle values, according to equation 24.

the impact of the slight wavelength difference, the simulated angle within the glass domain is inserted into Snell's law to calculate the also the refraction at the second interface, to be able to compare the results. After a second refraction of the wavefronts simulated in figure (19), angle values of 17.6° for metasurface A and 36.2° for metasurface B, which is a derivation of 1% from the experimental results. The impact of the wavelength difference is small.

For a further study of the metasurfaces' behaviour, an additional 70 nm thick layer of PC403, a polymer used for planarization layers (refractive index $n_{\mathrm{PC403}} = 1.5$) is spin coated on top of the gold nanorod pattern for both of the metasurfaces A and B. The results are shown in figure (21) in blue. The powers decreases approximately by a factor of 2, since the plasmonic resonance strength and wavelength position of the gold nanorods is sensitive to the refractive index of the surrounding medium. The resonance shift leads to a certain degree of off-resonance for the measured wavelength, addressing the conversion efficiency value at the peak flank instead of the peak maximum, which is significantly lower. This can be explained very well by the simulations shown in figure (17), which show the red shift of the resonance mode for an additional layer of larger refractive index on top.

Inversion of incident light direction It has been checked experimentally how the refraction angle changes if the light direction is changed. Therefore, the sample is rotated by 180° around the y-axis.
The refraction directions do not change at all, since the phase gradient of the pattern does not change its direction for this exact rotation, nor does the total refraction angle value change, which is also predicted by the theoretical calculation, leading to the same formula for both cases due to the switching of the initial medium refractive index with the final medium refractive index. The measurement setup is symmetric under sample rotation of 180° around the y-axis. The corresponding experimental results can be found in the supplement section at the end of this work in figure (41).

4.2 Double layer metasurface stack

The previously discussed single layer metasurfaces are combined within a double layer metasurface stack and investigated in the following section. At first the simulation results of stacked gold nanorod arrays are presented, afterwards the transition to stacked actual metasurfaces used for anomalous refraction is made, similar to the course of the single layer metasurface investigation.

4.2.1 Conversion efficiency of two stacked gold nanorod arrays

In this section the simulation results for a vertically stacked double layer gold nanorod array on top of a glass substrate will be presented. A schematic illustration is given in figure (22). The lower array is completely embedded in the glass half-space, while the upper array is on top of the glass surface and surrounded by air. The arrays are designed such that each center point of a rod in one layer is located directly underneath (or above, respectively) the center point of a rod in the other layer, meaning there is no horizontal shift between the upper and lower array. The vertical spacing S between the layers is measured from center to center of two vertically neighboring rods, the periodicity P is measured form center to center of two neighboring rods within an individual array and is always equal for both arrays. All rods within one array share the same polar angle, but the two rod arrays themselves may have individual angle values. Therefore, two degrees of freedom can be introduced, the polar angle of the rods in the upper and lower array, Φ_{up} and Φ_{low}, respectively. For symmetry reasons the degrees of freedom to describe all possible mutual array orientations reduce to 1 by introducing the relative angle $\Phi_{\text{rel}} \in [0; \pi)$ between the upper and lower array rods.

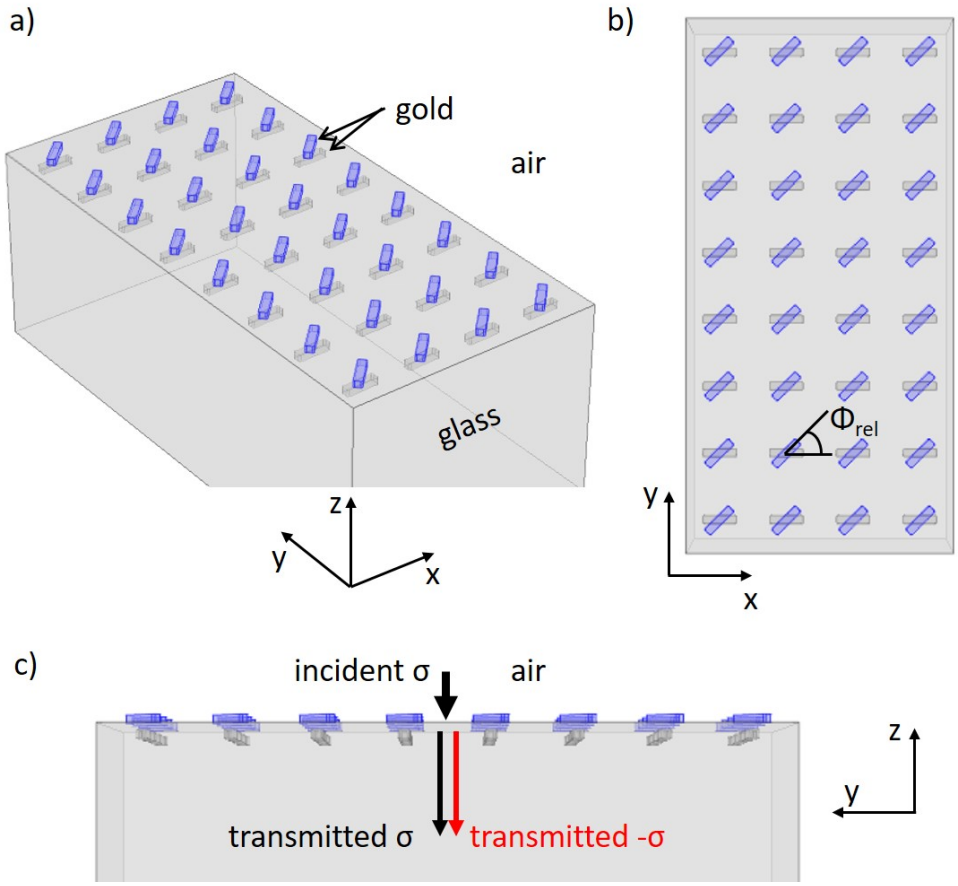

Figure 22: Schematic drawing of two vertically stacked gold nanorod arrays on a glass substrate in 3-dimensional view (a), top view (b) and side view (c). The upper array is located directly on top of the substrate, while the lower array is embedded in the substrate. The collective orientation angle of the gold rods in the upper array (blue) in respect to the collective orientation angle of the lower array rods (transparent) is described by the relative polar angle Φ_{rel}. Normal incident light of polarization σ (black arrow) is transmitted into the glass space, partly changing its polarization (red arrow).

The conversion efficiency for normal incident σ-polarized light, incident from the air half-space onto the stacked nanorod arrays, is simulated for different values of Φ_{rel} and shown in figure (23). The rods have the length $L = 200$ nm, the width $W = 50$ nm and height $H = 40$ nm. The periodicity within both layers is $P = 400$ nm, while the vertical spacing is $S = 70$ nm.

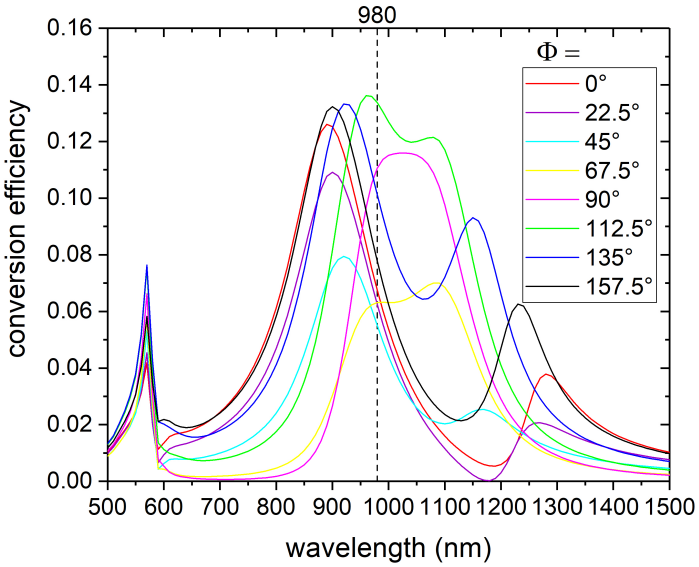

Figure 23: Simulated polarization conversion efficiency spectra for the stacked double layer gold rod arrays for different relative orientation angles Φ_{rel} in the visible and near-infrared range. The optimal experimentally available wavelength is indicated by the dashed line.

The spectra show different degrees of coupling between the vertically neighboring rods. The single LSPR-peak seen in the simulations of a single array now splits up into two distinct coupled modes, the symmetric and antisymmetric plasmon modes (see section 2.1) The symmetric mode is represented by the peak at lower wavelength. The peak height difference and the degree of splitting is dependend on the coupling strength between the rods, which is dependent on the relative orientation of the rods, described by Φ_{rel}. The strongest splitting is observed for $\Phi_{\text{rel}} = 0°$, decreasing as the angle approaches $\Phi_{\text{rel}} = 90°$, where no splitting is seen, increasing again to the initial

splitting value as Φ_{rel} approaches 180°. The parallel state of the stacked rod arrays have the highest coupling strength, while the perpendicular state of the two rod arrays show no coupling. The stronger the mode splitting, the more asymmetry of peak intensity is observed, showing constantly higher peak values for the lower wavelength symmetric mode, compared to the higher wavelength antisymmetric mode.

Parameter-optimization The single layer metasurface functionality relies on the equal conversion efficiencies for each different level used in the unit cell. To figure out an optimal wavelength for the case of the double layer metasurface stack, the coefficient of variation (CV) is evaluated for the conversion efficiency for each level (described by Φ_{rel} for the double layer configuration) and plotted against the wavelength in figure (24). The coefficient of variation is defined as the ratio between the standard derivation of a set of data points, and its mean, in this work's case,

$$\text{CV}(\lambda) = \frac{\text{std}(E_i(\lambda))}{\text{mean}(E_i(\lambda)} = \frac{\sqrt{8 \cdot \sum_{i=1}^{8} \left(E_i(\lambda) - \sum_{i=1}^{8} E_i(\lambda)\right)^2}}{\sum_{i=1}^{8} E_i(\lambda)}, \tag{33}$$

where the sum index i denotes the 8 different levels and E_i the corresponding conversion efficiency. It is used to quantify the suitability of fabrication and measuring parameters.
The minimal coefficient of variation corresponds to the optimal wavelength, because it provides the wavelength value of least conversion efficiency variation in regards to a certain value of conversion efficiency itself. A wavelength of $\lambda_0 = 980$ nm is chosen in the following, due to the experimental availability of a laser diode at this wavelength, even though it is not the wavelength of minimal CV value, but nevertheless close to it. At this optimal wavelength the mean conversion efficiency is evaluated to 0.084. The best mean conversion efficiency of the single layer simulations are 0.100 for the optimal wavelength. Therefore, the efficiency is expected to be slightly lower for the double layer array.
It should be kept in mind that this wavelength optimization process is highly dependent on the dimension of the rods, their periodicity within an array and the vertical spacing of the arrays as well. For this reason, these three parameters are varied, while keeping the wavelength of $\lambda_0 = 980$ nm fixed. This can be seen as a fine-tuning optimization step to the previously optimized

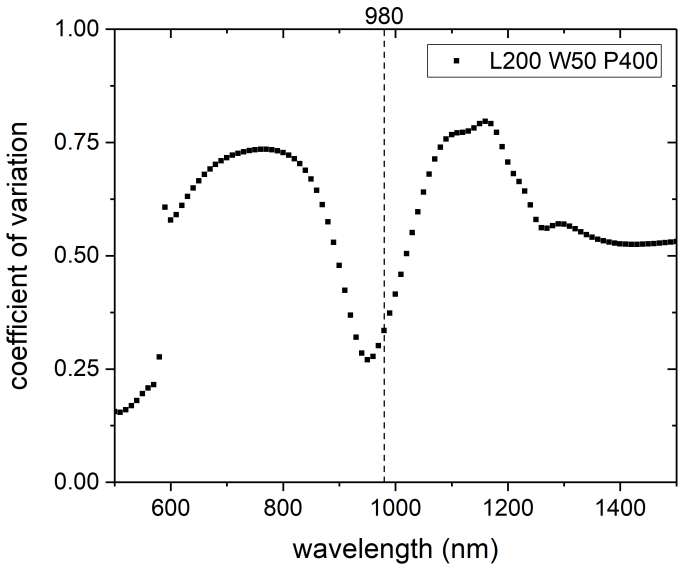

Figure 24: Evaluated coefficient of variation for the conversion efficiencies for the different relative rod angles, plotted against the wavelength. The optimal experimentally available wavelength, corresponding to the minimal CV value, is indicated by the dashed line.

wavelength. The most sensitive parameter will be the rod length. For this reason the conversion efficiency for each level is evaluated for various rod lengths and plotted against the length. An example is shown in figure (25) for $P = 400$ nm, $W = 50$ nm and $S = 70$ nm. This evaluation is repeated for several other values of the rod width W, the periodicity P and the vertical spacing S. The coefficient of variation is evaluated for each of the parameter sets and presented in figure (26).

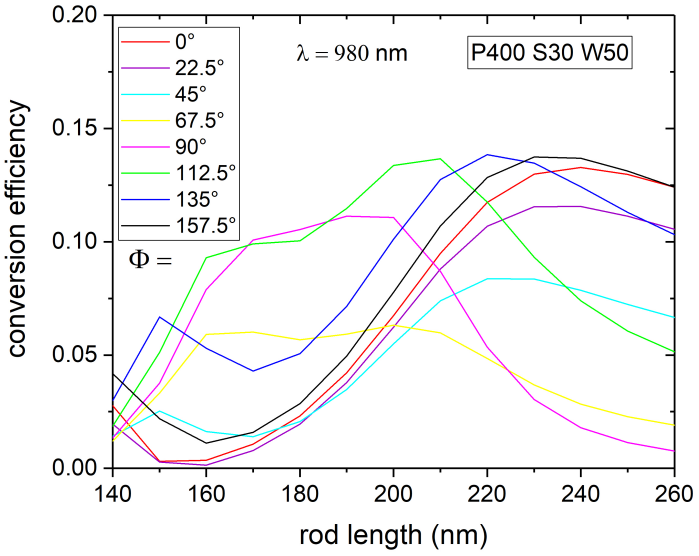

Figure 25: Simulated conversion efficiency for a fixed wavelength of $\lambda_0 = 980$ nm, plotted against the rod length L for different relative rod angles between the stacked nanorod arrays. The geometrical parameters are given in the form P400 S30 W50, where the letter represents the periodicity P, the vertical spacing S and the rod width W, respectively. The following number is given in the unit of nanometers. This form of presenting the geometrical parameters is adapted in following plots as well.

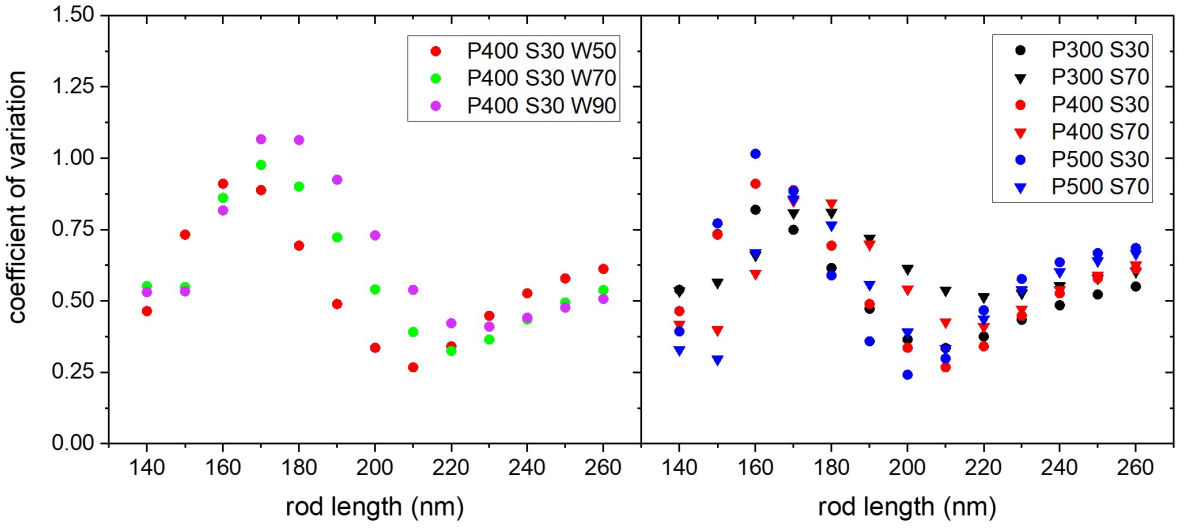

Figure 26: Evaluation of the coefficient of variation (CV) for fixed wavelengths $\lambda_0 = 980$ nm and different geometrical parameter values. The rod width W is varied while keeping the periodicity P and spacing S constant (left). The periodicity and the spacing are varied for the fixed width $W = 50$ nm (right). The optimal geometrical fabrication parameters are chosen with the help of the minimal CV evaluation.

On the left hand side W is varied for fixed $P = 400$ nm and $S = 30$ nm. The best parameter value (= minimal CV) can be evaluated to be the pair of $W = 50$ nm for a rod length of $L = 210$ nm. On the right hand side the width $W = 50$ nm is fixed, while the periodicity P and the vertical spacing S is varied. Again the best L can be found in the length range of 200-210 nm. For a rod length in this region, $S = 30$ nm shows the lower CV value results compared to $S = 70$ nm for every combination of periodicity. The CV does not depend on the periodicity P so strongly at these rod lengths. The result of the parameter optimization is $L = 210$ nm, $W = 50$ nm, $P = 400$ nm, $S = 30$ nm, for a fixed incident vacuum wavelength of $\lambda_0 = 980$ nm. The mean conversion efficiency for this set of parameters increased to 0.097, which is very close to the value of 0.100 for the best parameter choice of the single array case. In the end the final parameter values for the double layer metasurface stack are very close to the ones which are used to fabricate the single layer metasurface.

A further annotation should be made, that the choise $P = 500$ nm shows a slightly lower CV value than the choosen $P = 400$ nm, but since the ratio of P and λ_0 additionally should be kept low, in order to have the subwavelength spatial phase control, it was decided to go with $P = 400$ nm. The CV value additionally can be found to be low for a rod length of 150 nm. This parameter set was checked by simulations and found to be not working properly, which may be explained by the high degree of off-resonance (compare figure (25)) at these rod lengths. Some levels show very low conversion efficiencies and are not able to contribute to the scattered light at all. Additionally the low rod length values correspond to the position of the antisymmetric mode. For this work's concept it is important to use the symmetric mode, which will be explained in the course of the next section.

4.2.2 Phase shift dependence on Φ_{rel}

The key element of a metasurface is the dependence of the phase shift added to the incident light at a certain position (x,y) on the rod angle (level) at this position. For the two stacked nanorod arrays the levels of the individual arrays can take on arbitrary values and are independent from each other. The phase shift of polarization converted transmitted light for 8 different levels of the stacked array configuration with the optimized set of parameters is simulated and presented in figure (27).

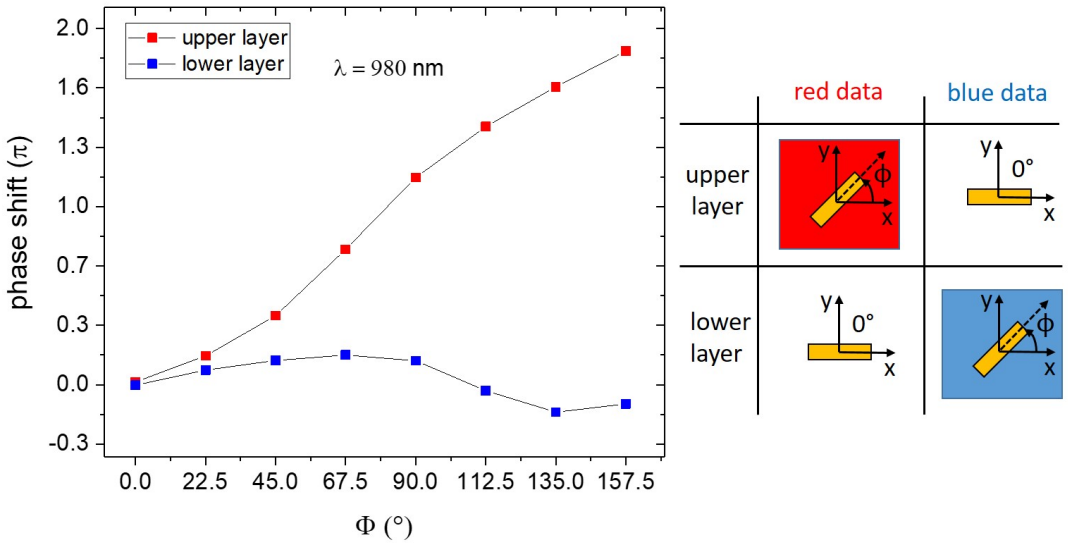

Figure 27: Simulated phase shift of the transmitted polarization converted light at the interface of the stacked double layer gold rod arrays for the optimal wavelength $\lambda_0 = 980$ nm. The values shown in red are received by rotating the upper array rod angle Φ_{up}, while keeping the lower array angle Φ_{low} constant 0°. The blue data is achieved by proceeding the other way round. The two layers show different behaviour of influencing the phase of the transmitted light.

The plotted upper array phase shift curve is received by successively rotating the upper array angle and evaluating the phase shift for each level value, while keeping the angle of the lower array constant 0°. The lower array phase shift curve is received the other way round: The upper layer angle is held constant, while the lower layer angle is set to the 8 different level values successively, performing a phase shift evaluation each.
Astonishingly the phase shift induced by rotating the two sets of rods is very different for the upper and lower array. The levels of the upper array show very similar phase profile compared to a single layer array: A (mostly) linear dependence of the phase shift of the polarization converted light on the rod angle, covering the complete phase interval $I_\phi = [0; 2\pi)$. The levels of the

lower array show very little influence on the phase shift, as their phase profile shows a flat run.
In the following we will speak of an 'active' layer, which is capable of controlling the phase of incident light (in this case the upper array) and an 'inactive' layer (in this case the lower array), which does not (or very little) influence the phase of light, independent from its level value. Furthermore, it can be observed, that the degree of inactivity, meaning the deviation of the phase shift profile from constant 0, is highly dependent on the fabrication parameters. If 'bad' parameters are chosen, corresponding to a high CV value, the degree of inactivity of the inactive layer as well as the degree of linearity of the active layer gets worse. The possibility for a double layer array to reach the phase profile quality of a single layer array, showing highly linear phase shift behaviour, rooting in the equal value of conversion efficiency for each level, is very questionable. It will not be possible to decouple the angle configuration of the double layer array from the conversion efficiency completely, but the evaluation of the optimized parameter set helped to get close to it.
A further interesting observation is the possibility of the upper array taking the role of the 'inactive' layer, while the lower array is the 'active' one. The layers switch roles so to say. The observation is made, that the roles of the two arrays are dependent on the incident wavelength and the position of the two resonance modes. A simulated phase profile graph is shown in figure (28) (left), as well as the corresponding conversion efficiency spectra (right) for the used levels. The geometrical parameters as well as the wavelengths are chosen such that the higher wavelength symmetric mode is addressed. The upper layer array shows the constant flat phase profile and forms therefore the inactive layer, while the lower layer array phase profile shows the linear bahaviour, indicating the active layer for this case.
If the incident wavelength corresponds to the position of the symmetric plasmonic mode (smaller wavelength, higher energy), the upper array plays the role of the 'active' layer, the lower array that of the 'inactive' layer. If the incident wavelength corresponds to the position of the antisymmetric mode (larger wavelength, lower energy), the array roles interchange and the lower array is the 'active' one, capable of influencing the phase of the transmitted light. This fact may be explained by the different degrees of localization of the two modes on one of the arrays.
In order to investigate the mode behaviour, figure (29) shows the electric field for the two wavelengths corresponding to the symmetric and antisymmetric mode of 4 different levels. The arrows' length represents the strength

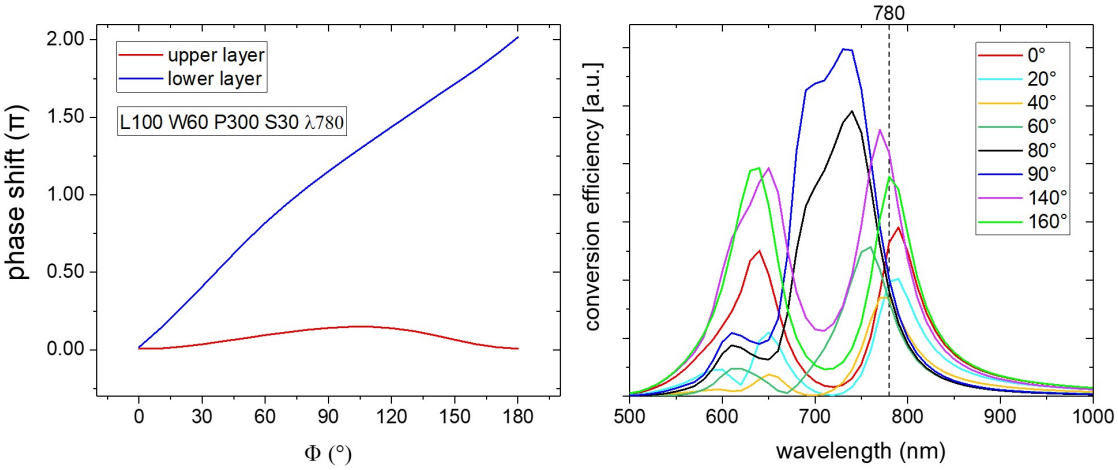

Figure 28: Simulated phase shift and conversion efficiency spectra for various levels of a geometrical design, which addresses the antisymmetric mode. The roles of the upper and lower layer arrays change, in respect to the evaluation of the design, which uses the symmetric mode.

of electric field at the center of a rod, their direction corresponds to the direction of electric field at this position. It can be observed, that indeed, the smaller wavelength mode, which is shown in the top line, shows electric fields with have the same direction within the lower and upper layer rod, while the higher wavelength mode, presented in the lower line, shows the electric fields pointing in opposed directions. This confirms and justifies the a priori chosen names 'symmetric' and 'antisymmetric' mode for the observed resonance peaks. The electric field leads to a charge motion and, dependent on the conductivity of the metal, to a certain current flow within the rods. The simulated observation therefore fit very well to the theoretical considerations of the LSPR-coupling scheme in the theory chapter, where we considered in-phase and antiphase electron motions and their mutual coulomb repulsion. For the perpendicular case of the two rod arrays, no peak splitting was observed in the conversion efficiency spectrum and it is not possible to distinguish between two modes. A further interesting observation is the fact that the symmetric mode plots, show larger electric field strengths within the upper array rods, while the antisymmetric mode behaves opposite. The symmetric mode is more localized on the upper array, the antisymmetric

mode is more localized on the lower array. A suggesting speculation is that the array, onto which the chosen mode is localized to a higher degree, takes the role of the active layer.

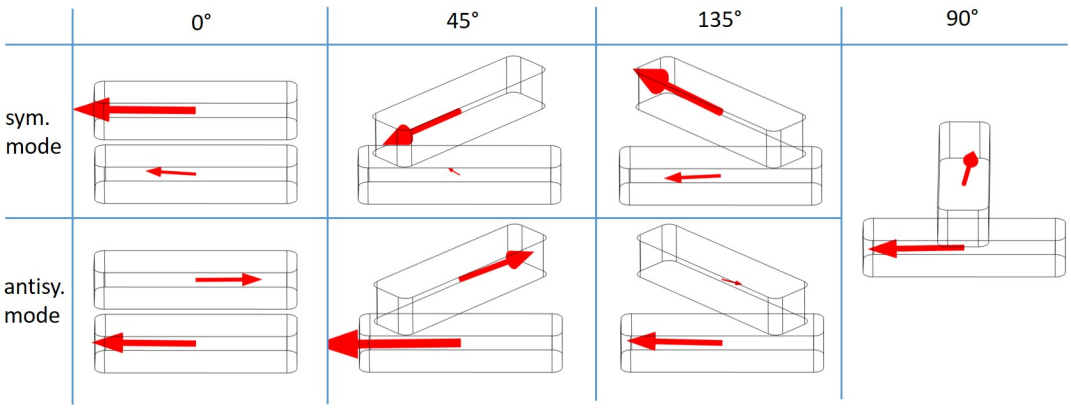

Figure 29: Simulated electric field for the symmetric and antisymmetric coupled plasmon modes for 4 different levels of the vertical gold nanorod array stacks. The red arrows' length is proportional to the strength of electric field at the tail position, which is chosen to be in the center of a rod. The direction of the arrow represents the direction of electric field. For the perpendicular case, there is no splitting in symmetric and antisymmetric mode.

4.2.3 Double layer metasurface stack for anomalous refraction

In this section the transition from the stacked gold nanorod arrays with collectively oriented rods to a configuration of two stacked actual metasurfaces is made. For each metasurface an individual phase gradient is designed. For simplicity the two phase gradients of the previous discussed single layer metasurfaces A and B are chosen, $\Delta\Phi = 22.5°$ and $\Delta\Phi = 45°$, corresponding to a unit cell length of $L_A = 3200$ nm and $L_A = 1600$ nm, respectively. A top view of the unit cell is shown in figure (30) at the top. On the left hand side the metasurface A forms the upper layer and B makes up the lower layer, while on the right hand side the roles are interchanged and the metasurface B is on top of A. The normalized electrical field for the transmitted polarization converted light in the xz-plane is depicted below for both cases. The normal incident light is circularly polarized with a wavelength of $\lambda_0 = 980$ nm. The dashed lines show a 12° and 25° reference line in respect to the x-axis. The black arrow represents the wave vector $\vec{k}$ of the reference wave front.

The phase shift evaluation has shown that only the upper layer will affect and spatially shift the phase of the incident light, meaning only the upper layer can function as a metasurface and refract the transmitted light accordingly. This is confirmed by the simulations, wherein the transmitted light is similarly refracted compared to the case of having just the upper layer single metasurface configuration (compare figure (19)), which can be seen at the reference wavefronts, which agree in angle which the single layer results. Nevertheless the wave fronts show some wavelike features and are not exactly planar. This may be due to the unequal intensity of the scattered spherical waves at each different level, making up the wave front by superposition. Even though the parameters are chosen, which showed the least variation of conversion efficiency between the different levels, the conversion efficiencies still differ to a certain degree (quantitatively described by their CV value), resulting in the observed non-ideal phase shift profile and ultimately to slightly non-planar transmitted wave fronts.

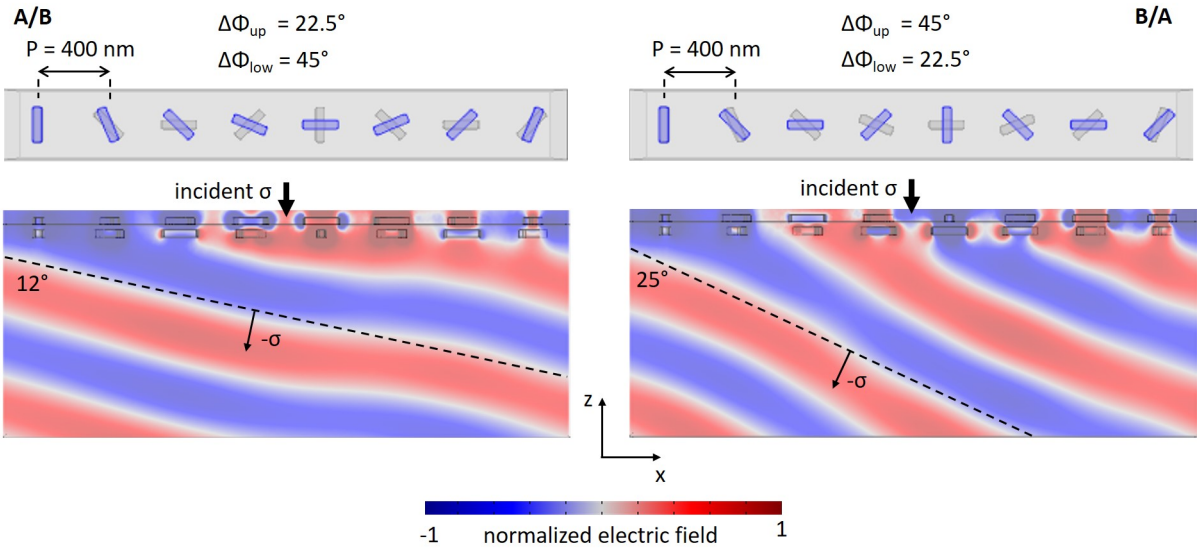

Figure 30: Simulated transmitted normalized electric field for the double layer metasurface stack, containing the individual metasurfaces A on top of B (left), and the opposite case of B on top of A (right). A unit cell top view of the metasurface stacks is shown on top, where the upper metasurface rods are shown in blue and the lower metasurface rods in transparent grey. The electric field is simulated in a side view perspective of the glass half-space below. The dashed lines represent 12° and 25° reference lines. The black arrows represent the direction of the wave vector of the reference light wave front.

Optimizing of wavefront quality Different combinations of phase gradients are used to optimize the wavefront quality. The two phase gradients for the two metasurfaces A and B ($\Delta\Phi = 22.5°$ and $\Delta\Phi = 45°$), as well as the corresponding x-inverted gradients ($\Delta\Phi = -22.5°$ and $\Delta\Phi = -45°$) are used. This will result in various different vertical configurations of two rods within the double layer unit cell. Figure (31 and 32) show the simulation results. Metasurfaces of same phase gradient value $\frac{\Delta\Phi}{P} = \frac{22.5°}{400nm}$ but inverse x-directions, on top of each other (A/A'), inverted gradients with same value of $\frac{\Delta\Phi}{P} = \frac{45°}{400nm}$ (B/B') and inverted gradients of different value (B/A') are simulated. The x-inverted metasurfaces are marked by a dash. The normalized electric field in the glass half-space is shown. A top view of the unit cell is given above, respectively. The wavelike features of the wave fronts seen previously for the first configuration (A/B) increase a lot for the (A/A') and the (B/B') case. For the (B/B') configuration the non-planarity of the wave fronts is even worse than for the (A/A') case. The (B/A') configuration shows better wavefront quality than (A/A') and (B/B'), but worse than (A/B).

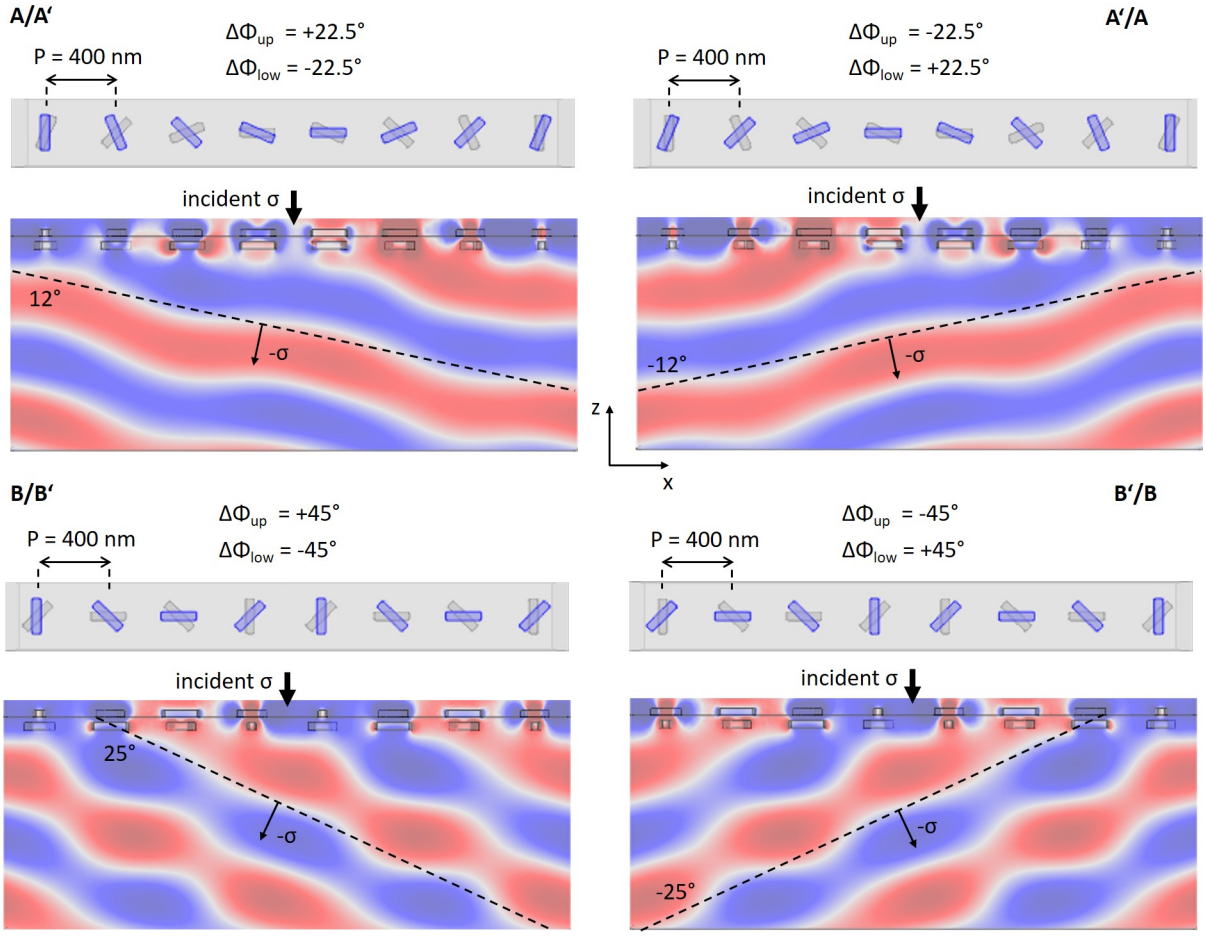

Figure 31: see figure 32 on the next page.

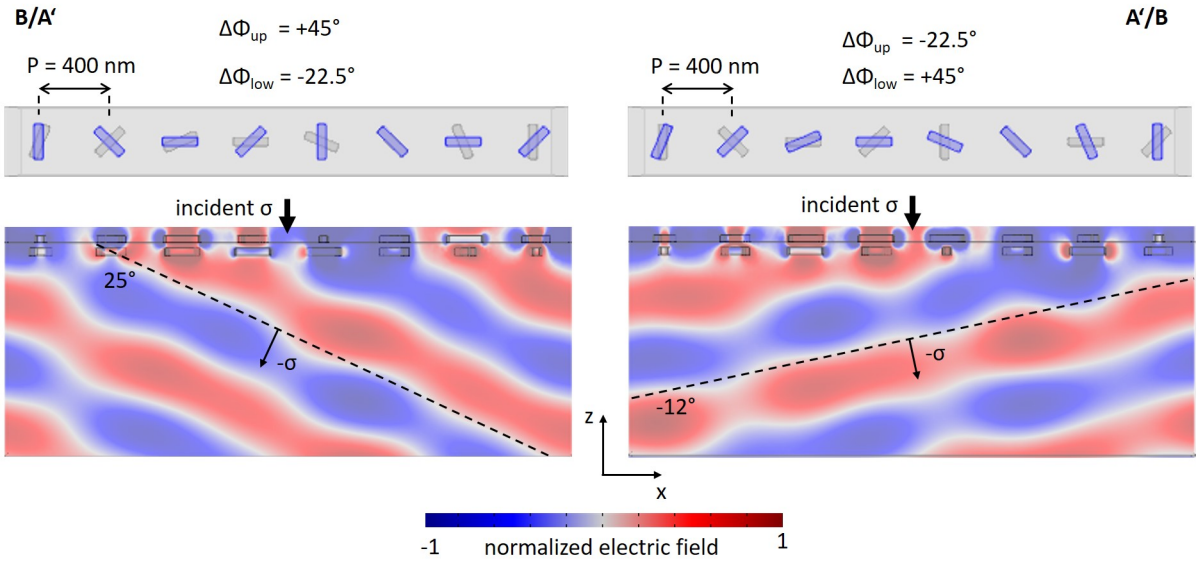

Figure 32: Simulated transmitted normalized electric field for the double layer metasurface stack, of different combinations of metasurface A and B and their x-inversions. The configuration with the positive gradient metasurface on top is presented on the left hand side, the negative gradient metasurface on top is shown on the right hand side. A unit cell top view of the metasurface stacks is shown above each simulation, respectively, wherein the upper metasurface rods are shown in blue and the lower metasurface rods in transparent grey. The electric field is simulated in a side view perspective of the glass half-space below. The dashed lines represent 12° and 25° reference lines. The black arrows represent the direction of the wave vector of the reference light wave front.

A closer look at the top view images of the unit cells for the configurations, points out that the (A/B) and (B,A') unit cell contains 8 different levels, the (A/A') unit cell contains 4 and the (B/B') only 2. If the CV is evaluated, taking not all of the 8 levels, but only 4 or 2, respectively, into account, it results in a larger value, meaning a larger discrepancy of the conversion efficiencies between the different contributing levels, resulting in partially non-planar superimposed wave fronts. The CV is evaluated for the discussed configuration and depicted in figure (33). It is observed that the 8 level configuration shows the lowest CV value, while the 2 level configuration shows the highest value, just coinciding with the observation that the (A/B) stack shows the best wave front quality and the (B/B') stack the worst one.

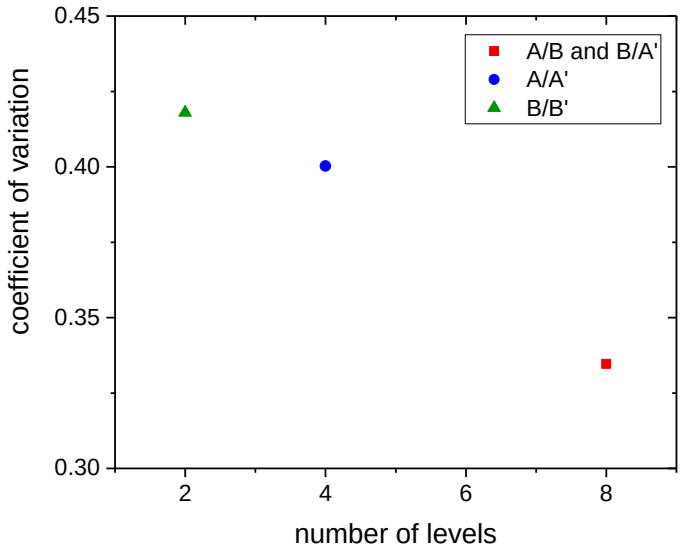

Figure 33: Evaluated coefficient of variation for three different numbers of levels in the unit cell of the simulated various double layer metasurface stacks.

To keep the two ideas, both metasurfaces refracting into opposite directions for the ease of experimental measurements, and simultaneously having 8 levels in the unit cell to contribute to the transmitted light waves, the configuration (B/A') is the most interesting. The wave front quality is better compared to the (B/B') and (A/A') case, but still is not reaching up to the quality of the first case (A/B). By maintaining the inverted gradients, which will simplify to distinguish the influence of the different layers during the optical measurements, the (B/A') case is the best compromise after all and fabricated in this work. Its simulation results shows a efficiency of 0.097, coinciding with the mean conversion efficiency of the 8 levels investigated with the help of the stacked array simulations. As the metasurface stack unit cell contains all 8 levels, this is found to be in good agreement with the expectation.

Experimental results The SEM-image of metasurface B on top of A' is shown in figure (34) on the left hand side, which will be referred to as metasurface stack 1. The interchanged configuration (A'/B) is depicted on the right hand side, named metasurface stack 2. Note that the rods of the underlying layer are slightly out of focus plane and appear to be thinner and less bright compared to the top layer. In reality they have the same dimensions, which was checked by SEM during the fabrication process of the first layer.

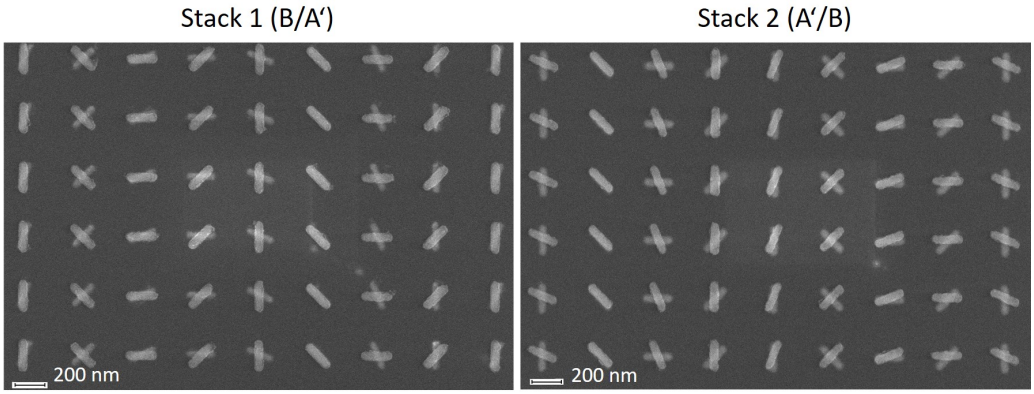

Figure 34: SEM-image of the metasurface stack 1, containing the metasurface B as top layer and A' as lower layer (left) and metasurface stack 2 with the interchanged layer configuration (right). The corresponding simulations are presented in figure (32).

The optical measurement of these two double layer metasurface stacks are carried out with the single wavelength measurement setup, which is described in the previous chapter 3.3 and also used to measure the previously discussed single layer metasurfaces. The normal incident wavelength is again $\lambda_0 = 980$ nm, the incident power $P_0 = 100$ μW. The angle dependent power of polarization converted, anomalous refracted light is investigated.

The results for the metasurface stack 1 and 2 are plotted in figure (35) in red colour, respectively. Two peaks are observed, which differ significantly in power. The angle values of both peaks agree with the refraction angle value of the individual metasurfaces contained in the double layer stack (compare equation 31 and 32). The peak, which corresponds to the individual metasurface on the top of each stack is always stronger than the one corresponding to the individual metasurface lying underneath, embedded in PC403. The single layer peak power for the individual metasurfaces A and B are marked by horizontal dashed lines. The layer stack is depicted as well, indicating the light direction by the yellow arrow.

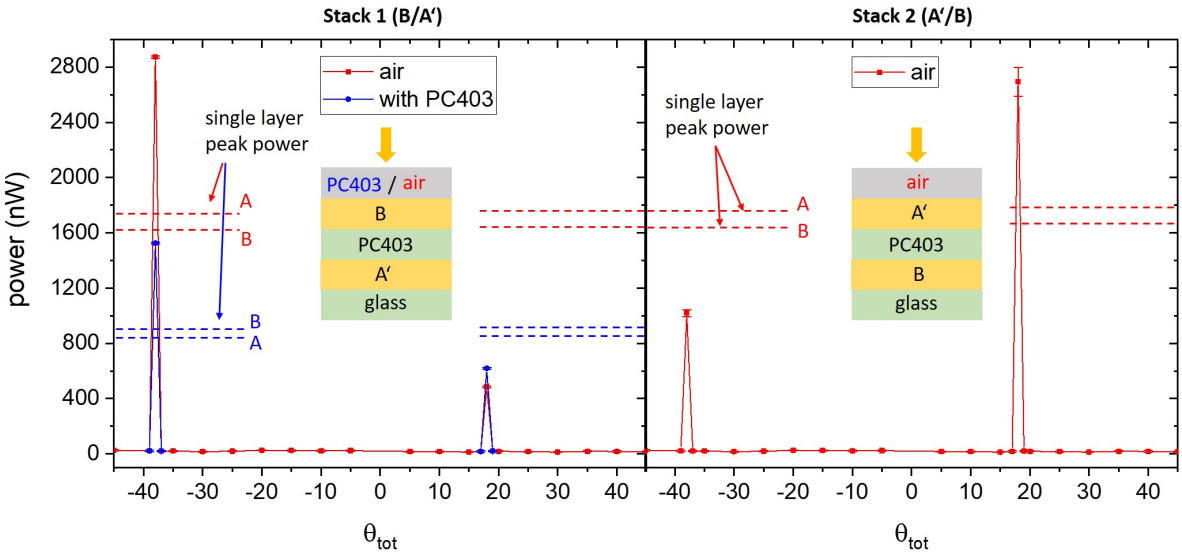

Figure 35: Graph of the angle resolved power of the light refracted by the metasurface stack 1 on the left hand side and metasurface stack 2 on the right hand side, for initial medium air (red) and initial medium PC403 (blue). For metasurface stack 2 the PC403 investigation is not shown. The layer stack is shown, indicating the light direction by the yellow arrow and the initial medium in grey. The individual single layer metasurfaces' peak power is marked by horizontal dashed lines for metasurface A and B for air (red) and PC403 coating (blue).

Remarkably the optical response of the metasurface stack is not the simple sum of both, the individual metasurfaces A and B on the first glance. Rather the total incident power is split up onto the individual directions in a asymmetric manner. The power transmitted into the direction corresponding to the top layer metasurface is larger than that of the individual metasurface, for same fabrication parameters, area, laser power and wavelength. Meanwhile the power fraction measured in the direction corresponding to the lower layer (embedded in PC403) is smaller than the power measured for the individual single layer metasurface, embedded in PC403 as well.
The asymmetric splitting of peak power strongly hints at the coupling of the two metasurfaces, resulting in a contribution of conversion efficiency of the lower layer to the total converted and refracted light, but since the lower layer is not able to influence the phase, the direction is solely given by the upper layer. Due to the decoupling of phase shift and conversion efficiency the lower layer contributes to scatter light into the direction of the upper layer, independent of its phase distribution design.
It should be noted, that the optimized set of parameters for the double layer metasurface stacks are not the optimal parameters for the individual single layer metasurfaces, since the coupling shifts the resonance position. Therefore it appears that the metasurface stack shows even better efficiencies than a single layer metasurface, which is probably not the case if one chooses a appropriate wavelength for the single layer measurements as well. For the optical measurements of the single layer metasurfaces A and B the measurement wavelength does not correspond to the peak maximum but to a position on its flank, since all the parameter adjustments are done for the stacked two layer case. A shift of 50 nm away from the optimal wavelength for the single layer metasurface simulations depicted in figure (15) shows a conversion efficiency of 70% of the peak value.
The overall transmitted power (sum of the two peaks) is 3356 ± 8 nW for metasurface stack 1 and 3711 ± 107 nW for stack 2. This result is in good agreement with the sum of the transmitted power of both the individual metasurfaces, which is 3383 ± 134 nW. This result is actually not predicted by the simulations, which have shown a mean conversion efficiency value very close to that of a single layer metasurface measured at its optimal wavelength. As the measured configuration contains all 8 levels in the unit cell, the mean conversion efficiency of these levels should be able to represent the efficiency of the metasurface stack itself, which is then expected to be similar to the single layer metasurface value, not twice its value. It might be explained

by the degree of off-resonance measuring position for the single layer metasurfaces, if we assume a efficiency drop by a factor of 2 due to off-resonant measuring of the single layer metasurfaces.
The objective of this work is that the coupling between two vertically stacked metasurfaces results in an electromagnetical cloaking of the lower metasurface. A complete cloaking of the lower metasurface was not possible in the experiment. There might be the possibility to further improve the cloaking of the lower surface by increasing the coupling efficiency between the two layers by further optimization of the fabrication parameters. A compelte cloaking requires a constant 0 phase shift profile for the lower layer. This is only achieved by equal and level independent conversion efficiencies, which is difficult to achieve, since the level configuration itself is influencing the coupling strengths of the rods, which determines the conversion efficiency of the respective level.

PC403 coating A further study in which the double layer stack 1 is coated with another 70 nm thick layer of PC403 on top of the upper layer, embedding both layers in PC403 environment, lead to the measurement results shown in figure (35) in blue. The peak of the upper layer changes in power approximately by a factor of 2, similar to the behaviour of the coated single layer metasurface studied before. The power of the lower layer stays the same, since the surrounding medium is still the PC403 layer of the initial fabrication and therefore unchanged. As seen before the loss in power is attributed to the red shifting of the resonance peaks for increased refractive index, resulting in a off-resonant measuring wavelength position on the flank of the peaks. Remarkably, the peak power of the upper layer of the stack coated with the additional layer of PC403 on top, is still significantly larger than the power of the individual single layer metasurface coated with PC403 as well. There may be the previously suggested explanation, that the coupling leads to a scattering contribution of the lower metasurface into the direction of the upper one, increasing its peak power compared to the individual single layer peak power for same surrounding medium.

Open questions At the end the question has to be asked, if the intensity difference between the two power peaks, observed for the optical measurements of the metasurface stack in the directions of the contained individual

metasurfaces, may also be explained for the assumption of no coupling of the contained metasurfaces. A suggestion would be a different degrees of shifting of the resonance peaks for both individual layers, away from the measuring wavelength position, by either the individual fabrication error of the rod length ΔL or the slight difference in refractive index of the two surrounding media PC403 and glass. It might be possible that the PC403 layer underneath the upper metasurface layer makes a significant refractive index difference, compared to ITO-glass. It might shifts the upper metasurface resonance of the stacked configuration in a beneficial way compared to that of the individual single layer metasurface fabricated directly on ITO-glass, so that a larger power is measured into that direction. An open question will be, if the significant power loss of the lower metasurface peak can be attributed simply to fabrication errors of the rod length between the two samples, leading to another off-resonant shift. Only a single sample was fabricated in this work, so the statistical errors might have a non-neglectable impact. The simulations predict a total power transmission for the stacked case to be similar to one individual metasurface measured at its optimal wavelength. The twice as lager total power value for the stacked configuration might be another hint that it is just a sum of two (partly resonance shifted) individual single layer metasurfaces in different surroundings. At the end, these questions can not be answered with the help of the to date gathered experimental data. Nevertheless, the data demonstrates that the coupling and cloaking of the lower layer indeed is possible to a significant degree. This paves the way to achieve beam steering into two arbitrary and switchable directions, if phase change materials are used. The concept is presented in the following.

4.3 Switchable metasurface stack for light beam steering

A post-processing dynamic of the double layer metasurface stack can be achieved by using magnesium rods within the upper layer metasurface instead of gold rods. The lower layer still consists of gold rods. The latter results show that the light which incides on the layer stack is controlled by the upper layer only (compare figure (27)). It is possible to address the lower layer, if the first metasurface gets 'inactivated' somehow, meaning the prevention of coupling and resonant scattering of the incident light wave. This can be achieved with the help of the phase transition of magnesium (metallic state) to magnesium-hydrid (dielectric state) upon hydrogen exposure of magnesium. The process of hydrogenation is reversible upon oxygen exposure, which is important to make the device switchable back and forth [15][3][8][7].
If the upper layer material is magnesium in its metallic state, the incident light is resonantly scattered and refracted according to the level distribution within the upper layer metasurface. If the magnesium layer is exposed to hydrogen, forming the dielectric material magnesium hydrid, the incident light passes the upper layer without coupling and subsequently interacts with the lower layer gold metasurface, being refracted according to its (different) level distribution. Since both the level distributions in the two layers are independent from each other, the light beam direction can be steered to two different directions upon hydrogen and oxygen exposure, respectively, adding a post-processing dynamic to the metasurface stack, which cannot be achieved with a single layer metasurface.
The concept is illustrated step-by-step in figure (36). First a metasurface stack is considered containing two gold metasurfaces fabricated with a phase gradient which refracts the light into direction A. In the second step, the upper metasurface is exchanged for a magnesium metasurface, designed to refract the incident light to another direction B. The whole stack refracts the light according to the upper magnesium metasurface, since the lower gold metasurface is not able to influence the phase of the light, which is the key element of the reported concept and heavily investigated and discussed in the previous sections. The third step shows how to switch back the light direction to A. Upon hydrogen exposure, the magnesium rods undergo a phase transition to magnesium hydrid, which is a dielectric material. The light does not interact resonantly and just passes through to the lower gold meta-

surface, which now is not cloaked anymore, since the cloaking effect roots in the coupling of the two layers, only possible for metal particles. The light is therefore refracted according to the lower layer phase distribution into direction A again. The hydrogenation process is reversible upon oxygen exposure, which will switch the magnesium hydrid back to the metallic magnesium and therefore steers the light beam direction back to B.

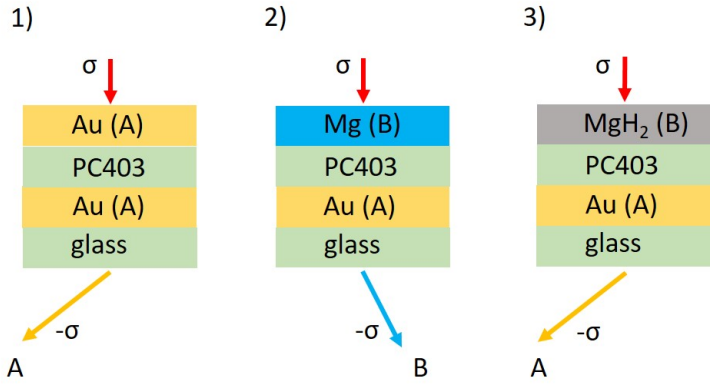

Figure 36: Step-by-step illustration of developing the concept for switchable deflection directions with the help of a Mg/Au metasurface stack. For two stacked gold metasurfaces of design A, the final light direction is given by A (1). After exchanging the top layer for an magnesium based metasurface of design B, the final light direction is given by B, since the lower layer is cloaked (2). If the magnesium undergoes the phase transition to magnesium hydrid, the light passes through the first metasurface without interaction and incides on the lower gold metasurface, which is not cloaked anymore, resulting in the final light direction given by A again (3).

4.3.1 Conversion efficiency and phase shift of Mg/Au metal-hybrid array stack

The conversion efficiency spectrum is simulated for an inital parameter set of $L = 200$ nm, $W = 50$ nm, $P = 400$ nm and $S = 30$ nm, and presented in figure (37a), the corresponding coefficient of variation is evaluated and shown below (b). The minimal CV value is achieved for a wavelength of 800 nm as well as for a wavelength of 1200 nm, corresponding to the symmetric and antisymmetric coupled plasmon modes, respectively. The concept of the

switchable metasurface stack is that if the Mg-metasurface is in the 'active' state, it must have the role of the 'active' layer. This means a wavelength has to be used which corresponds to the position of the symmetric mode of the coupling spectrum, because at this wavelength, the upper metal array defines the 'active' layer, solely capable of influencing the phase, as we have seen in the previous studies for two stacked gold arrays.

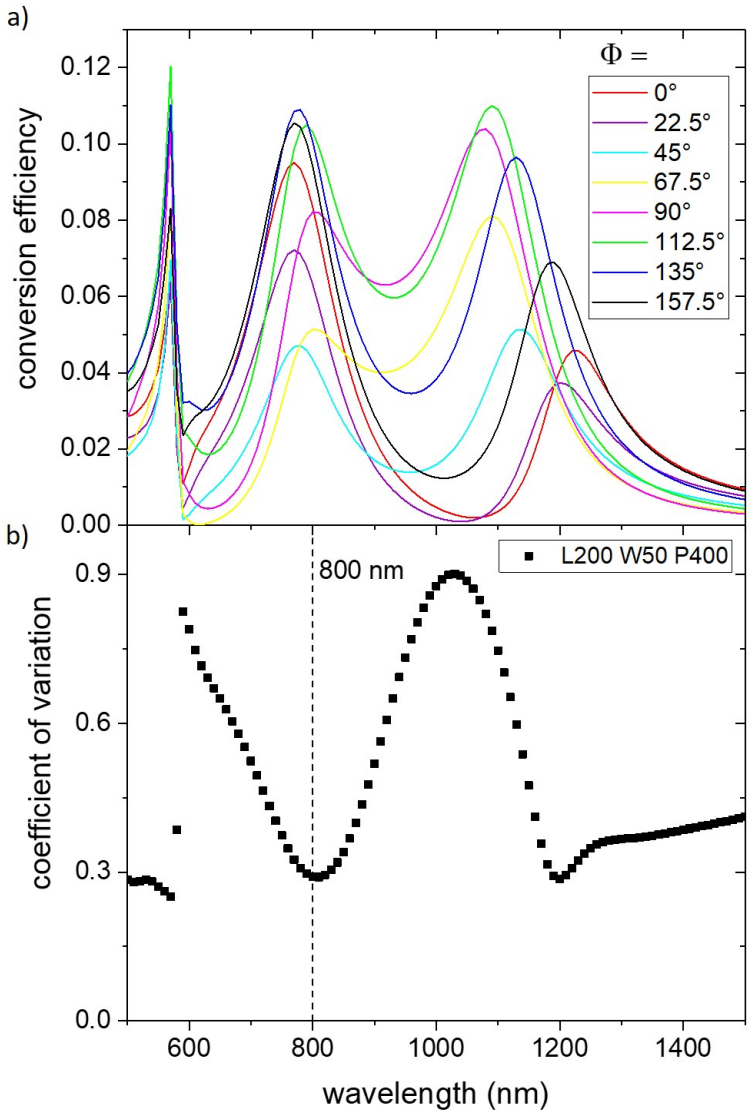

Figure 37: Simulated polarization conversion efficiency spectra (a) for the Mg/Au rod array stack for different relative orientation angles Φ_{rel} in the visible and near-infrared range. The lower wavelength peak is the symmetric coupled plasmonic mode. Corresponding evaluated coefficient of variation (b) for the 8 different relative rod angles in (a). A low value indicates a good wavelength choice.

To be able to use the experimentally available wavelength of $\lambda_0 = 980$ nm, the rod length is varied, such that the symmetric mode moves to the given wavelength. The result is shown in figure (38a) and the corresponding CV evaluation below (b). The geometric parameters are $P = 400$ nm, $W = 70$ nm and $S = 30$ nm. The width is increased for the ease of fabrication of the magnesium metasurface, since magnesium is more difficult to handle than gold for small dimensions. The peak at larger rod lengths corresponds to the symmetric plasmon mode. The minimal CV value for the symmetric mode is found to be achieved for a rod length of $L = 270$ nm for this set of parameters. Note that the antisymmetric mode peak at $L = 150$ nm shows a low CV value, but it cannot be used for the concept, since the roles of the active and inactive layers are interchanged.

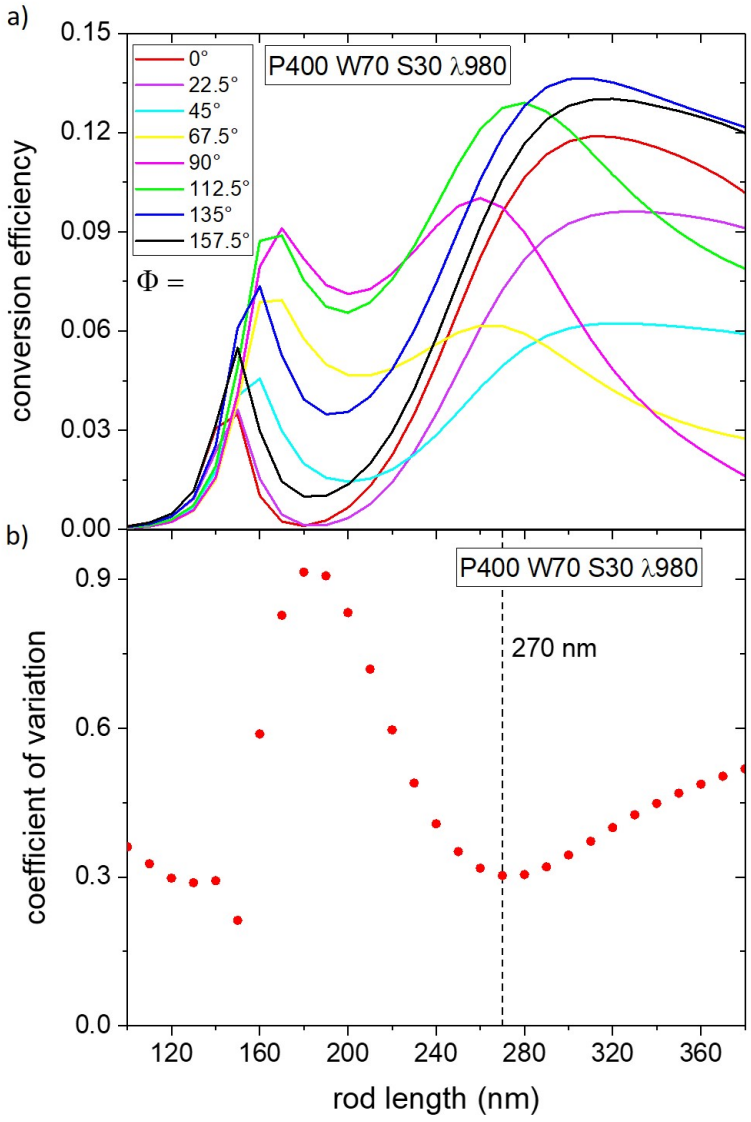

Figure 38: Simulation of the conversion efficiency for the 8 different levels for a fixed wavelength of $\lambda_0 = 980$ nm, plotted against the rod length (a). The peak at larger lengths corresponds to the symmetric mode. Evaluated coefficient of variation for the rod length variation (b). A low value indicates a good rod length choice.

A phase shift simulation is performed for the evaluated optimized parameters and plotted in figure (39). Therefore the phase shift of the polarization converted transmitted light for the stacked metal nanorod array is simulated for a rotation of the magnesium rods in the upper array, while keeping the gold rods of the lower array at constant 0° angle (red) and the other way round (blue). The result is similar to the case of two gold arrays. The upper layer (Mg-layer in this case) is able to influence the phase, showing a linear dependence on the rod angle over the complete phase interval, and therefore forms the 'active' layer. The lower layer (Au-layer in this case) does not influence the phase of transmitted light much, as a nearly constant 0 phase shift profile is seen, and therefore forms the 'inactive' layer. The lower 'inactive' layer is supposed to influence the phase of light only if the magnesium rods of the upper layer change to magnesium hydrid rods upon hydrogen exposure.

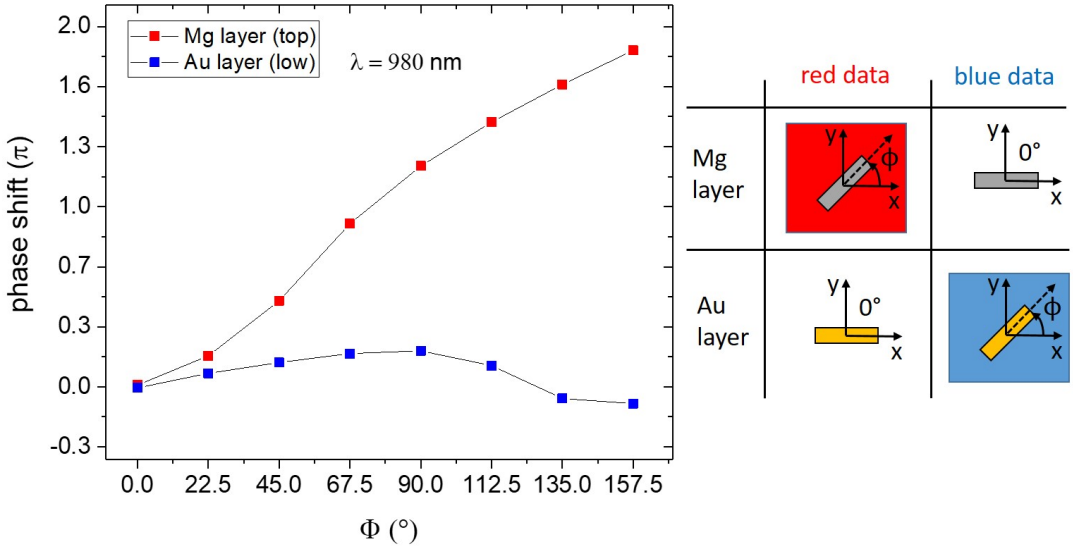

Figure 39: Simulated phase shift of the transmitted polarization converted light at the interface of the Mg/Au array stack for the optimal parameters $\lambda_0 = 980$ nm and $L = 270$ nm. The values shown in red are received by rotating the magnesium (grey) array rod angle Φ_{Mg}, while keeping the gold (yellow) array rod angle Φ_{Au} constant 0°. The blue data is achieved by proceeding the other way round. The two layers show different behaviour of influencing the phase of the transmitted light, similar to the previous investigation of two stacked gold arrays.

4.3.2 Simulations of Mg/Au metal-hybrid metasurface stack

The simulated electric field of the polarization converted transmitted light of the Mg/Au hybrid metasurface stack is shown in figure (40) for the configuration of (B/A'), wherein the individual metasurface B is made out of magnesium rods (left) and forms the top layer, while metasurface A' forms the lower layer and contains gold rods. On the right hand side, the magnesium rods of the upper layer are exchanged by magnesium hydrid.

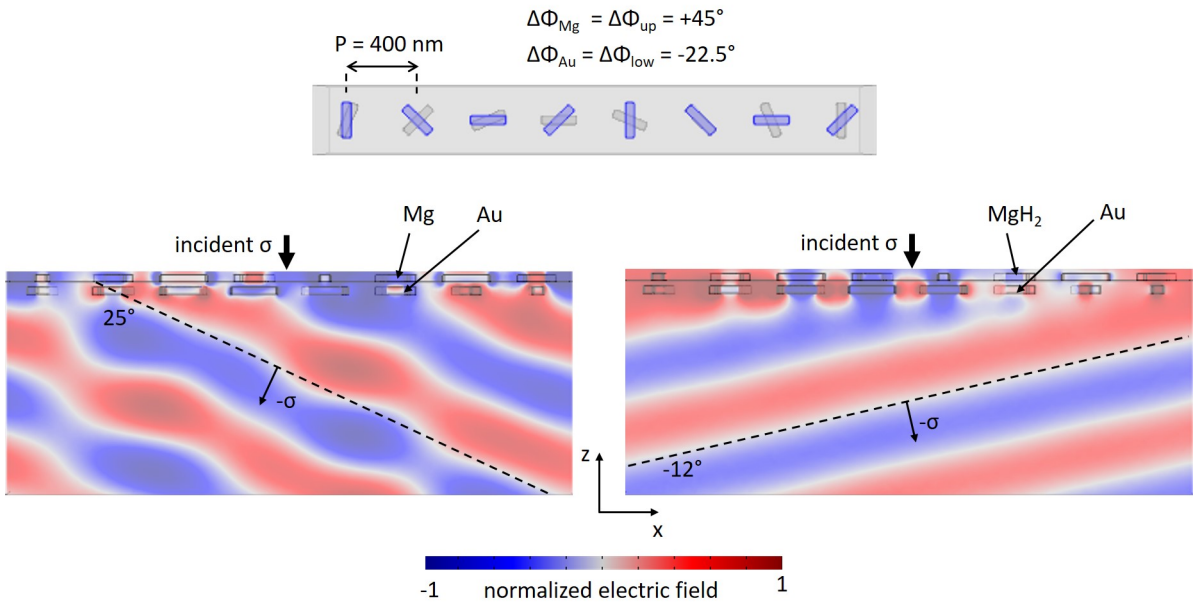

Figure 40: Simulated normalized transmitted electric field for the Mg/Au metasurface stack, containing the Mg-metasurface B as top layer and a x-inverted Au-metasurface A' as lower layer. A unit cell top view of the metasurface stack is shown on top, wherein the magnesium rods are shown in blue and the underlying gold rods in transparent grey. The electric field is simulated in a side view perspective of the glass half-space below for the Mg-metasurface in the metallic state (left), as well as for the dielectric magnesium hydrid case (right). The dashed lines represent 12° and 25° reference lines. The black arrows represent the direction of the wave vector of the reference light wave front.

The wave fronts for the metallic state of the Mg-metasurface show the wave-like features, similar to the previously studied case of the gold metasurface stack. Nevertheless the wave front angle agrees very well with the expected value, which is that of the individual single layer Mg-metasurface (compare equation 31 and 32). The cloaking of the lower layer works also for the Mg/Au-hybrid metasurface stack, with comparable quality.
The wave fronts of the dielectric state of the upper metasurface are observed to be planar and in very good agreement with the simulations of the individual single layer gold metasurface. The light only interacts with the lower gold metasurface. The simulation results show that the developed concept of the Mg/Au-hybrid metasurface stack is very likely to work as intended.
The next step to further investigate the idea has to be the fabrication of a individual Mg-metasurface B, the individual Au-metasurface A' covered with PC403, as well as the latter described stacked configuration (B/A'). With the help of optical measurements of these three designs one will be able to characterize and evaluate the potential functionality of the concept. These investigations are left open to a follow-up work.

5 Summary, Conclusions and Outlook

In this work a concept for a post-processing dynamic metasurface has been developed and investigated. The metasurface consists of two layers, which are individual single layer metasurfaces itself, stacked on nanometer distance above each other. It is shown in theory that a incident light beam can be steered into two different arbitrary and switchable transmission directions by changing the geometric phase.

At first individual single layer gold based PB-metasurfaces are investigated in terms of simulations as well as experiment. It was shown that the anomalous refraction with such gold-based single layer metasurfaces is possible, which relies of the concept of spatial phase control by the polar angle of the gold nanorods on the metasurface and a simultaneously independent scattering efficiency for each rod from its angle adjustment.

Thereafter, a double layer gold metasurface stack is designed and investigated by theory and experiment, which contains the individual metasurfaces designed for anomalous refraction, stacked on a 70 nm distance above each other on top of a glass substrate. The experiment shows that incident light is anomalous refracted mainly to the direction attributed to the design of the upper layer metasurface, independent from the design of the lower layer metasurface. The lower layer metasurface can be considered as 'electromagnetically hidden' to a certain degree by the upper one. This behaviour is attributed to the coupling of the rods of each layer and the different embedding environment of each individual metasurface. It is observed that the total scattering efficiency of the stack is made up of contributions of both layers due to the coupling, while the direction of the scattering is solely determined by the upper layer. The degree of cloaking of the lower layer metasurface direction might be increased by inducing a better coupling between the two layers by appropriate design improvements.

There are several observed problems, which root in a single basic problem. The conversion efficiencies of the double layer levels (relative angle between upper layer and lower layer rods) differ significantly. The reason why a single layer metasurface works well, relies on the equal conversion efficiency, completely independent of the level (rod angle). The transmitted wavefronts of polarization-converted light are seen to be not exactly planar for the metasurface stack, but showing wavelike features, which root in the phase shift profiles of the two layers. The phase shift dependence for the upper layer levels shows derivations from a desired linear profile, the phase shift de-

pendence of the lower layer shows derivations from a desired flat constant 0 profile. The lower layer then has a significant influence on the phase of the light, resulting in the experimental observation of scattered intensity according to the lower metasurface refraction direction. It was shown that a parameter optimization, aiming for smallest variation of conversion efficiencies between the levels, optimizes the phase shift profiles of the two layers, ultimately leading to an improvement of the wavefront quality. Probably it will be difficult to improve the design to account for a equal conversion efficiencies for all possible levels, since the light scattering is attributed to the coupled particle plasmon modes, which show very different conversion efficiencies for the various levels. This is because the coupling strength, which determines the conversion efficiency, is dependent on the level configuration itself. It is therefore questionable if a complete hiding of the lower metasurface refraction direction is possible. Nevertheless, the experimental results are satisfying, as they show a clear intensity difference between the two individual metasurface refraction directions, as desired.

The observed difference in influence on the transmitted light by the two layers of the gold metasurface stack is used to design a metasurface stack, which is capable of switching the incident light beam to two arbitrary directions. This can be realized by exchanging the upper layer gold rods by magnesium rods. The Mg-metasurface, in contrast to the gold metasurface, can be switched 'on' and 'off'.

Simulations of the hybrid-metal metasurface stack containing Mg-metasurface for the upper layer and a gold-metasurface for the lower layer show the light refraction attributed to the design of the magnesium metasurface, independently of the design of the underlying gold metasurface. Furthermore, simulations of the stack, exchanging the magnesium rods by magnesium hydrid rods, show the light refraction according to the design of the gold metasurface. The refraction can be switched from Mg-metasurface refraction to gold-metasurface refraction upon hydrogen exposure, as well as switched back to Mg-metasurface refraction upon oxygen exposure, which adds a post-processing dynamic to the metasurface stack.

For the described concept of beam steering by a double layer metasurface stack, it is necessary to have the upper metasurface 'hiding' the lower one. During the investigation of the gold metasurface stacks it is shown, that for selecting appropriate wavelengths, corresponding the the antisymmetric coupled plasmon modes, the roles of the metasurface can be interchanged, meaning the lower metasurface 'hides' the upper one (for same incident light

direction). This observation is very interesting and promising for adding another post-processing dynamical aspect to the metasurface stack in the future.

Supplement

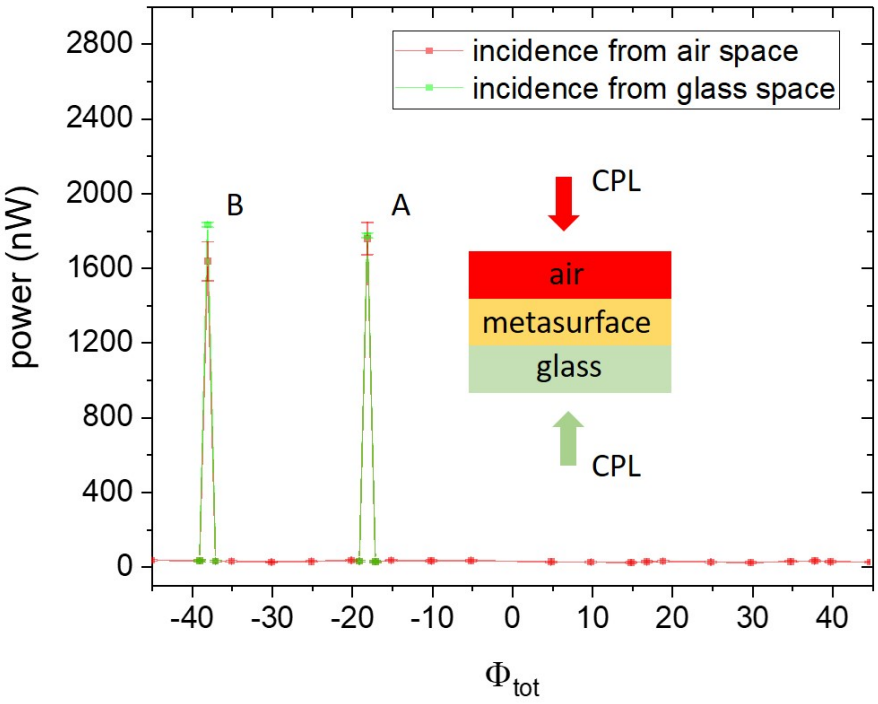

Figure 41: Angle dependent power measurement for the inversion of the light path for the single layer metasurfaces A and B. The angle as well as the power does not change for both of the metasurfaces A and B. The measurement process is symmetric under flipping the sample.

Acknowledgement

I want to thank Prof. Dr. Laura Na Liu for the opportunity to work in her group and do the research, which led to this thesis, Prof. Annemarie Pucci for the co-examination, as well as Dr. Frank Neubrech and Dr. Jianxiong Lee for the supervision and discussion of the results. Furthermore, I want to thank the remaining group members for their various support, especially Simon Kamin, who introduced me to the important experimental methods. At the end, I want to thank my family for supporting my graduation in physics.

References

[1] Amir Arbabi and Andrei Faraon. Fundamental limits of ultrathin metasurfaces. *Scientific Reports*, 7:1–6, 2017.

[2] Amir Arbabi, Yu Horie, Mahmood Bagheri, and Andrei Faraon. Dielectric metasurfaces for complete control of phase and polarization with subwavelength spatial resolution and high transmission. *Nature Nanotechnology*, 10(11):937–943, 2015.

[3] A. Baldi, G. K. Pálsson, M. Gonzalez-Silveira, H. Schreuders, M. Slaman, J. H. Rector, G. Krishnan, B. J. Kooi, G. S. Walker, M. W. Fay, B. Hjörvarsson, R. J. Wijngaarden, B. Dam, and R. Griessen. Mg/Ti multilayers: Structural and hydrogen absorption properties. *Physical Review B - Condensed Matter and Materials Physics*, 81(22):1–10, 2010.

[4] Jie Cao, Tong Sun, and Kenneth T.V. Grattan. Gold nanorod-based localized surface plasmon resonance biosensors: A review. *Sensors and Actuators, B: Chemical*, 195:332–351, 2014.

[5] Hou Tong Chen, Antoinette J. Taylor, and Nanfang Yu. A review of metasurfaces: Physics and applications. *Reports on Progress in Physics*, 79(7):76401, 2016.

[6] Salman Daniel, Kimmo Saastamoinen, Toni Saastamoinen, Ismo Vartiainen, Ari T. Friberg, and Taco D. Visser. Surface Plasmons Carry the Pancharatnam-Berry Geometric Phase. *Physical Review Letters*, 119(25):1–5, 2017.

[7] Xiaoyang Duan, Simon Kamin, and Na Liu. Dynamic plasmonic colour display. *Nature Communications*, 8:1–9, 2017.

[8] J. A. Dura, S. T. Kelly, P. A. Kienzle, J. H. Her, T. J. Udovic, C. F. Majkrzak, C. J. Chung, and B. M. Clemens. Porous Mg formation upon dehydrogenation of MgH2thin films. *Journal of Applied Physics*, 109(9), 2011.

[9] Susie Eustis and Mostafa A. El-Sayed. Why gold nanoparticles are more precious than pretty gold: Noble metal surface plasmon resonance and its enhancement of the radiative and nonradiative properties

of nanocrystals of different shapes. *Chem. Soc. Rev.*, 35(3):209–217, 2006.

[10] Qingbin Fan, Pengcheng Huo, Daopeng Wang, Yuzhang Liang, Feng Yan, and Ting Xu. Visible light focusing flat lenses based on hybrid dielectric-metal metasurface reflector-arrays. *Scientific Reports*, 7:1–9, 2017.

[11] Lingling Huang, Xianzhong Chen, Holger Mu, Guixin Li, and Benfeng Bai. Dispersionless Phase Discontinuities for Controlling Light Propagation. *Nano letters*, 12:5750–5755, 2012.

[12] Lingling Huang, Xianzhong Chen, Holger Mühlenbernd, Hao Zhang, Shumei Chen, Benfeng Bai, Qiaofeng Tan, Guofan Jin, Kok Wai Cheah, Cheng Wei Qiu, Jensen Li, Thomas Zentgraf, and Shuang Zhang. Three-dimensional optical holography using a plasmonic metasurface. *Nature Communications*, 4(May):1–8, 2013.

[13] Marek Piliarik, Pavel Kvasnička, Nicolle Galler, Joachim R. Krenn, and Jiří Homola. Local refractive index sensitivity of plasmonic nanoparticles. *Optics Express*, 19(10):9213, 2011.

[14] Carsten Sönnichsen. Plasmons in metal nanostructures. *Dissertation*, 27(June):134, 2001.

[15] Florian Sterl, Nikolai Strohfeldt, Ramon Walter, Ronald Griessen, Andreas Tittl, and Harald Giessen. Magnesium as novel material for active plasmonics in the visible wavelength range. *Nano Letters*, 15(12):7949–7955, 2015.

[16] Pin Chieh Wu, Wei-Yi Tsai, Wei Ting Chen, Yao-Wei Huang, Ting-Yu Chen, Jia-Wern Chen, Chun Yen Liao, Cheng Hung Chu, Greg Sun, and Din Ping Tsai. Versatile Polarization Generation with an Aluminum Plasmonic Metasurface. *Nano Letters*, 17(1):445–452, 2017.

[17] Nanfang Yu, Patrice Genevet, Mikhail a Kats, Francesco Aieta, Jean-Philippe Tetienne, Federico Capasso, and Zeno Gaburro. Light Propagation with Phase Discontinuities Reflection and Refraction. *Science*, 334(October):333–337, 2011.